THE STARRY MESSENGER

The Global Society of Young Physicists | Issue 4| August 2025



RMP

Applications of Quantum Mechanics

Gravitational Lensing

Modeling Neutron Star Matter: A Relativistic Mean Field Approach

Computational Modeling of Vibrational Analysis via Geophone Detection: Simulating Seismic Resonance and Frequency Spectra

ISSN: 3061-9807

Welcome to the fourth Issue of "The Starry Messenger", the triannual science magazine of the Global Society of Young Physicists (GSYP). I am truly excited to introduce the incredible work of our students from the recently concluded Research Mentorship Programme (RMP) 2025. This issue features three outstanding research reports that delve into the frontiers of modern physics, with one more to be published in December:

1. **Applications of Quantum Mechanics**
2. **Gravitational Lensing**
3. **Modeling Neutron Star Matter: A Relativistic Mean Field Approach**
4. **Computational Modeling of Vibrational Analysis via Geophone Detection: Simulating Seismic Resonance and Frequency Spectra**

The Global Society of Young Physicists (GSYP) was founded with a vision to connect young physics enthusiasts worldwide, fostering a community dedicated to advancing physics education. GSYP is a registered community interest company that supports budding physicists through a range of initiatives, including the Research Mentorship Programme (RMP), where students are paired with experienced mentors to undertake challenging research projects.

After five intense weeks, we concluded the RMP 2025, marking an incredible journey for all involved. As the Chief Executive Officer of GSYP, co-creator and lead coordinator of this programme, I had the privilege of guiding our brilliant students through their research projects. Serving as a mentor for the Quantum Mechanics course, I led a group of five passionate and brilliant students through five weeks of intensive lectures and research.



ISSN: 3061-9807

Throughout the programme, our students demonstrated exceptional dedication and curiosity, exploring complex topics such as Schrödinger's equation, quantum tunnelling, Bell's inequality, and even black hole information theory. Their efforts have culminated in remarkable research, just as the other teams.

The foundation of GSYP and the RMP was established through a personal experience that fueled my passion for research and education. Years ago, at a summer school on Quantum Cryptography at the University of Waterloo, I met like-minded individuals, including my dear friend and colleague Leo Nagel, who is the Senior Advisor at GSYP. Leo and I took the initial steps in founding GSYP, while embarking on a research project titled "Measurement of Thermal Conductivity of Thin and Thick Layer Graphene via Phonon Dispersion by Inelastic X-Ray Collision Produced Through Bremsstrahlung Radiation." As a team we had to work on this project without a mentor. The experience of working without a mentor underscored the importance of guided support for students undertaking research projects for me, laying the groundwork for what would become GSYP and the RMP.

This experience then inspired the creation of GSYP and the RMP, which aims to provide young physics enthusiasts with the mentorship and resources we lacked. Today, I am immensely proud of the outstanding work our students and mentors have accomplished. I would like to extend my thanks to the distinguished mentors of RMP 2025, and now fellows of GSYP: Nikita, Kajol and Ginevra; and senior fellows of GSYP: Toby and Piyamini. Last but not least, I would like to thank our students, now RMP Alumni, who made all of this possible. Thank you for all your hard work.

As always, we as GSYP encourage you to support and join our mission to further physics education and connect young physics enthusiasts worldwide. For more information, please refer to our posters at the end of our magazine.

Arya Lal Gonullu, Chief Executive
arya.gsyp@gmail.com



Become a Member of GSYP!

As a member of GSYP, you gain access to exclusive benefits that will enhance your journey as a young physicist. Members can request reviews from research mentors who are conducting cutting-edge studies in Physics. After a thorough editorial review, you can submit your work for publication in our science magazine. Additionally, you will have the opportunity to attend talks by renowned science experts brought in by GSYP.

Membership is currently free, so join us and take advantage of these incredible opportunities.

Science Magazine Schedule

Our Science Magazine will be published three times a year:

- **April**: Independent research published before the annual RMP.
- **August**: Research reports from the annual RMP.
- **December**: Independent research published after the annual RMP.

Stay tuned for our next issue in December 2025, where we will feature more research reports and provide details on the upcoming RMP 2026!

KEEP IN TOUCH!

GSYP Instagram: @gsyphysics

GSYP LinkedIn: https://www.linkedin.com/company/gsyphys/

GSYP YouTube, watch the Final Day Presentations for RMP 2025 here: https://youtu.be/3vN3LgSooXo



ISSN: 3061-9807

CONTENTS

FEATURES

5 Applications of Quantum Tunnelling

28 Gravitational Lensing

44 Modeling Neutron Star Matter: A Relativistic Mean Field Approach

59 Computational Modeling of Vibrational Analysis via Geophone Detection

REGULARS

58 Photos from RMP 2024

73 RMP 2026 Applications Open for Research Mentors! - Poster & Link

75 Photos from RMP 2025

76 Become a GSYP Member! - Poster

77 Become a Marketing Associate or Editor of The Starry Messenger! - Poster

78 Contributions

We invite you to become a GSYP member and take the first step towards your research dreams. Access expert talks, publish your research, and connect with a global community of young physicists. Don't miss out on this incredible opportunity to unlock your potential as a physics researcher.

The views of our writers are their own.
We aim for sound science but not editorial orthodoxy.

ISSN: 3061-9807

“Applications of Quantum Tunnelling”

Authors: Ruben Davies, Donia Mahmoud, Lucian Valman, Justin Wang, Lim Jun Hong

Research Mentor, Collaborator: Arya Lal Gonullu



ISSN: 3061-9807

Abstract

This report researches the phenomenon of quantum tunnelling applications in modern physics, engineering and electronics. Quantum tunnelling is a direct consequence of the wave-particle duality as described in quantum mechanics, which enables particles to pass through potential barriers without having sufficient energy, a phenomenon that is not possible according to classical physics. Applications such as the Scanning Tunnelling Microscope (STM) and tunnel diodes are discussed to show the practical application of quantum tunnelling effects in the real world.

1.0 Introduction

It is first important to define quantum tunnelling in the context of quantum mechanics. While classical mechanics maintains that an object cannot reach the other side of a barrier it does not have the energy to surmount, when introducing the wave particle duality inherent in quantum mechanics, this changes. The time-sensitive Schrodinger equation:

$$i\hbar\frac{d}{dt}|\Psi(t)\rangle = \hat{H}|\Psi(t)\rangle \quad (1)$$

describes a wavefunction's evolution with time. As the absolute value of this wave function is directly proportional to the probability distribution of observed points as shown by

$$|\psi(x,t)|^2 = \psi^*(x,t)\psi(x,t) = \rho(x), \quad (2)$$

where $\rho(x)$ indicates the probability density of a measurement of a particle's position at time t. As shown in Figure 1, when a wave-function described by the above equations impinges on a barrier, most of it is reflected but some is transmitted to the other side. This can be seen through an alternate form of the Schrodinger equation:

$$\frac{d^2}{dx^2}\Psi(x) = \frac{2m}{\hbar^2}M(x)\Psi(x) = -k^2\Psi(x) \quad (3)$$

Where $\hbar = \frac{h}{2\pi}$ and $M(x)$ is defined by $V(x) - E$ (a particle's energy in the *x*-axis subtracted from its potential energy) and is constant and negative. Solutions to these

ISSN: 3061-9807

equations are travelling waves with phase-constant k or $-k$. Where $M(x)$ is constant and positive, the equation can be written as:

$$\frac{d^2}{dx^2}\Psi(x) = \frac{2m}{\hbar^2}M(x)\Psi(x) = k^2\Psi(x) \quad (4)$$

As the sign of $M(x)$ can be said to define the medium through which the wave propagates, it follows that a region of positive $M(x)$ sandwiched between two regions of negative $M(x)$ constitutes a potential barrier. Through this, it is also possible that coupling occurs between the evanescent waves on either side of the barrier, thus constituting quantum tunnelling.

The wave also, therefore, becomes more delocalised as it now exists with lower maximum amplitude and on both sides of the barrier. However, as its integrated square-magnitude remains equal, the probabilistic certainty that the particle is detected somewhere is retained.

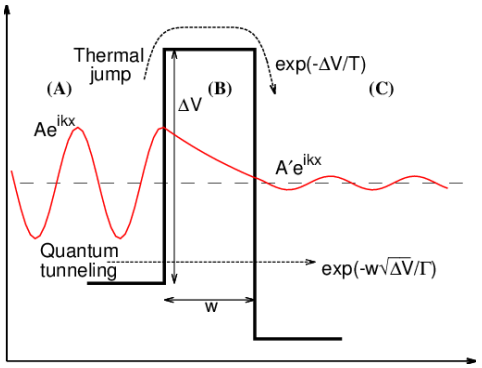


Figure 1: A diagram showing a wave function colliding with a barrier and being partially transmitted via quantum tunnelling

This shows that, through quantum effects, a wave function (and thus a measured particle) can be transmitted through a physical barrier without surmounting it in the classical sense.

The probability of tunneling can be approximated using this equation:

$$T \approx e^{-2\kappa d} \quad (5)$$

Where d is the distance the particle tunnels through and **κ** can be expressed as:

ISSN: 3061-9807

$$\kappa = \sqrt{\frac{2m(\phi - E)}{\hbar^2}} \quad (6)$$

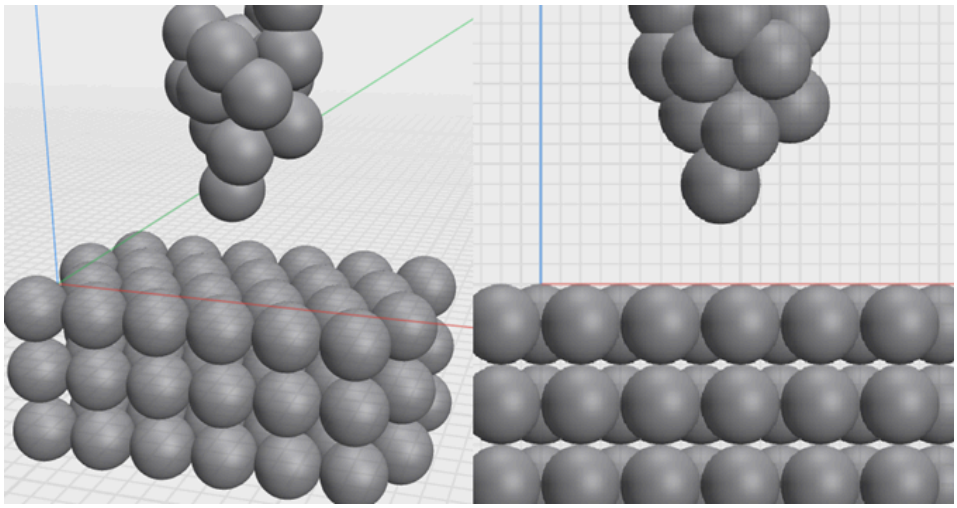
$\phi - E$ expresses the energy barrier the particle needs to overcome, m is the mass of the particle.

1.1 Introduction - STM microscope

One of the applications of quantum tunneling is STM telescope, or scanning tunneling microscope, which uses the method of detecting tunneling current to deduce the distance between the surface and the probe, which produces the image that has atomic resolution, in other words, it is an instrument that can be used to observe the surfaces of material at atomic level. Based on the concept of quantum tunneling, the microscope relies on detecting tunneling current from the object that is being observed (which has to be conductive). The magnitude of the current is indicative for the distance between the probe and the sample surface, therefore, creates an image like a contour map.

A potential difference will be applied between the probe and the surface for the electron to tunnel. In order to capture images with atomic resolution, the probe's tip must be made up of one single atom. The electron will exceed the potential barrier (the gap between the probe and the surface of the sample) and reach the atom at the tip of the probe, and it will not be lost because it is attracted by the nuclei (which is due to the positively charged nucleus being attractive to negatively charged electrons).

Figure 2 – The probe's tip of 1 atom approaches the surface of the sample



ISSN: 3061-9807

From equation (5), The probability of tunnelling, T reduces as d, the distance between the probe and the surface of the material, increases. With **κ** as a constant, we can deduce d from the tunneling current detected in the probe, as

$$I \propto T \approx e^{-2\kappa d} \quad (7)$$

1.2 Introduction - Nanocapacitors

Nanocapacitors can achieve far higher capacitance as well as storing and releasing charge faster compared to regular capacitors [1]. However, effects due to quantum tunnelling can pose a limit for how small they can become. Capacitors function with a pair of conductive electrodes separated by an insulating dielectric layer, which has high polarizability. This allows it to store charge after a voltage is put across it as one plate becomes positively charged and one becomes negatively charged, allowing it to release energy as current similarly to a battery. In nanocapacitors, both the electrodes and the dielectric can be only a few nanometres thick, and research has shown that capacitors with a dielectric with a thickness of only one atom give very similar results to capacitors without an insulating layer at all [2]. This is due to the potential well not being large enough to prevent quantum tunnelling of electrons between the electrodes, resulting in the capacitor being short circuited.

While quantum tunnelling is often an obstacle in the context of nanocapacitors, recent research has shown that quantum tunnelling effects can be used to increase the capacitance of certain types of capacitors. This is done by cooling them to extreme temperatures, where charges are injected into the dielectric layer by applying a strong electric field, through field emission tunnelling [3].

1.3 Introduction - Tunnel Field-Effect Transistor (TFET)

Another application of quantum tunnelling is Tunnel Field-Effect Transistor (TFET). TFET is an experimental transistor to reduce power consumption which uses the quantum mechanical band-to-band tunneling instead of using thermionic emission which is applied in the conventional MOSFET [5].

In conventional MOSFET, carriers are required to gain energy that is greater than the barrier height to overcome potential barrier to flow from source to drain when gate is

ISSN: 3061-9807

triggered. Besides, higher gate voltage is needed (>60 mV/decade switching), which is known as the thermal limit [6] for conventional MOSFET. On the other hand, carriers can have energy that is less than barrier height but still go through the barrier through quantum tunnelling while lower gate voltage (<60 mV/decade switching) is required [6].

2. Method

2.1 Method - STM microscope

For STM microscopes, sensitivity is one of the most important factors when evaluating its effectiveness. The energy waste is usually ignored because it is negligible, and most of its contribution would be from the external circuit. To show that STM can produce image with atomic resolution, we can sub in values in a process shown below:

In order to reach atomic resolution, we can investigate the current change when *d* varies by $0.01nm$.

$$\frac{\Delta I}{I} = e^{2\kappa\Delta d} - 1 \tag{8}$$

where κ can be approximated as

$$\kappa = \sqrt{\frac{2m(\phi - E)}{\hbar^2}} = \sqrt{\frac{2\times 9.11\times 10^{-31}\times(4.4\times 1.6\times 10^{-19})}{(6.63\times 10^{-34}\times\frac{1}{2\pi})^2}} \approx 1.07 \times 10^{10} \tag{9}$$

$$\frac{\Delta I}{I} = e^{2\kappa\Delta d} - 1 \approx 0.239 \tag{10}$$

This means that for every $0.01nm$ chane in d the current vary by 23.9%.

However, the STM cannot only work with solely a probe that remains in a fixed position. In order to gain fine control over the probe (i.e., enabling it to move in all three directions over distances that are smaller than the diameter of atom), it is necessary to make use of piezoelectric ceramics, applying voltage to such material would cause faint deformation on atomic scale, thus, would allow fine movements. The ceramic plate is usually divided into four regions, applying different voltages to different regions can enable movements in the *x* and *y* direction, uniform voltage applied in the two halves can enable movements in the *z* direction (up and down). This is closely related to an effect called piezoelectric effect, which describes the phenomenon that when a certain type of material deforms, it would generate a potential difference, and the inverse of this effect, also known as the inverse piezoelectric effect, is applied by the STM microscope, i.e., applying potential

ISSN: 3061-9807

difference to cause deformation. Notice that when the potential difference is removed, the material would return to its original shape. Materials with this property are called piezoelectric materials.

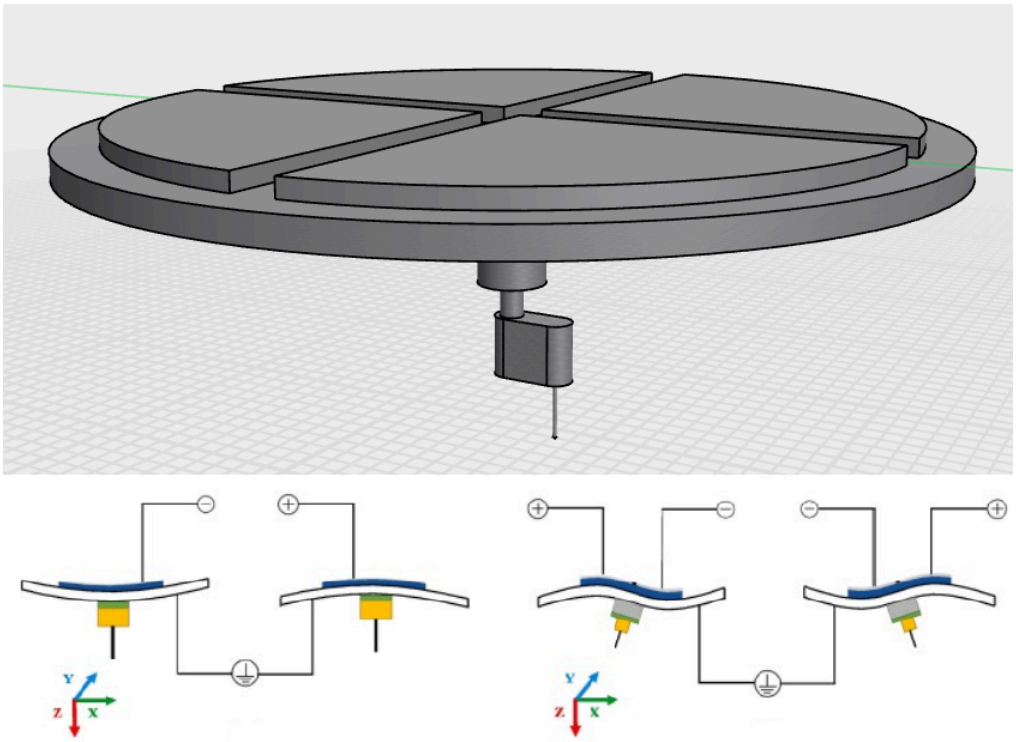


Figure 3 - ceramic plate with probe head attached to it, with movement mechanisms

Finally, a coarse adjustment system is required for the movements on millimetre and micrometer levels. In order to achieve this, a three-axis adjustment platform with screws and springs is needed, as shown below.

ISSN: 3061-9807

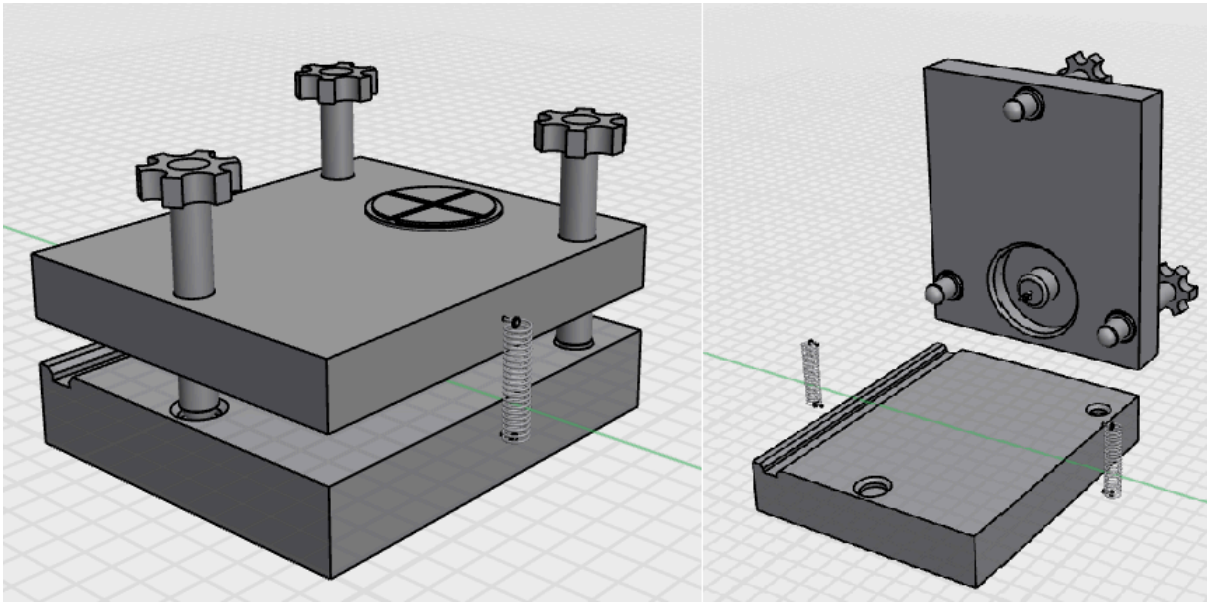


Figure 4 - Three-axis adjustment platform

2.2 Method - Nanocapacitors

This method uses Field emission tunnelling, a phenomenon where a strong electric field is applied to a metal, allowing electrons to escape from its surface in a process known as Fowler-Nordheim tunnelling. As an electron approaches the surface of the metal from the inside, the probability of it escaping (or "transmission coefficient") can be calculated as a function $D(h, F)$ of the distance to the barrier *h* and the barrier field *F*. It can be modelled by the following approach [4]:

$$G(h, F) = g \int M^{\frac{1}{2}} dx \tag{11}$$

Where the integral is taken across the barrier region, M(x) is as defined in equation (12) and g is a universal constant given by

$$g = 2\sqrt{2m}/\hbar \approx 10.24624 eV^{-1/2} nm^{-1} \tag{12}$$

For simple models:

$$D \approx e^{-G} \tag{13}$$

ISSN: 3061-9807

This equation is very similar to the general tunnelling probability equation (5), but more specific as it gives the probability as a function of field strength as well as distance. This shows how the transmission coefficient of a metal can be calculated when placed in a strong electric field.

Researchers at the University of Illinois has applied this phenomenon to increase the capacitance of nanocapacitors made from aluminium electrodes and an aluminium oxide (Al_2O_3) dielectric, with a thickness of only a few nanometres. When using these materials, electrons can be injected into the dielectric due to the substantial density of electron traps, areas which electrons can occupy in a low energy state. This means the injected electrons remain stable inside the dielectric provided the temperature is sufficiently low such that the conductivity of the dielectric is negligible. When the temperature is increased, electrons can diffuse through the dielectric and the trapped charge is released to the nearest electrode plate. In order to achieve successful charge storage on the dielectric, the electrons must be distributed asymmetrically. If this is managed, once the temperature increases, more electrons will flow to one electrode than the other, creating a discharge current and thus a release of energy. Such an asymmetric distribution can be created through field emission. Additionally, such a technique is only possible on nanocapacitors as they can tolerate substantially higher electric fields before the dielectric layer is damaged.

In order to perform this technique, the nanocapacitor is cooled to 77K and a voltage is placed across it. This charges the capacitor in the standard way, through the dielectric being polarised and the electrodes becoming charged. However, the resulting electric field between the electrodes, causing field emission from the electrodes. At this temperature, electrons can be stored stably in the dielectric layer, causing it to become asymmetrically charged over time, allowing more energy to be stored. The amount of energy stored in the dielectric depends on the charging voltage, as shown in Figure 2 [3].

2.3 Method - Tunnel Field-Effect Transistor (TFET)

In TFET, the source and channel are separated by a narrow tunnelling barrier. When gate voltage is applied, the energy bands bend enough to allow electrons to tunnel directly from the valence band of the source to the conduction band of the channel. Therefore, quantum tunnelling initiates current flow, even when the gate voltage is below

ISSN: 3061-9807

the conventional voltage threshold. Besides that, the probability of quantum tunnelling occurrence depends on barrier width and height, not temperature. This makes TFET become ideal for low-power electronics, as lowering the barrier height and width can significantly increase tunnelling probability and thus reduce the required switching

voltage.

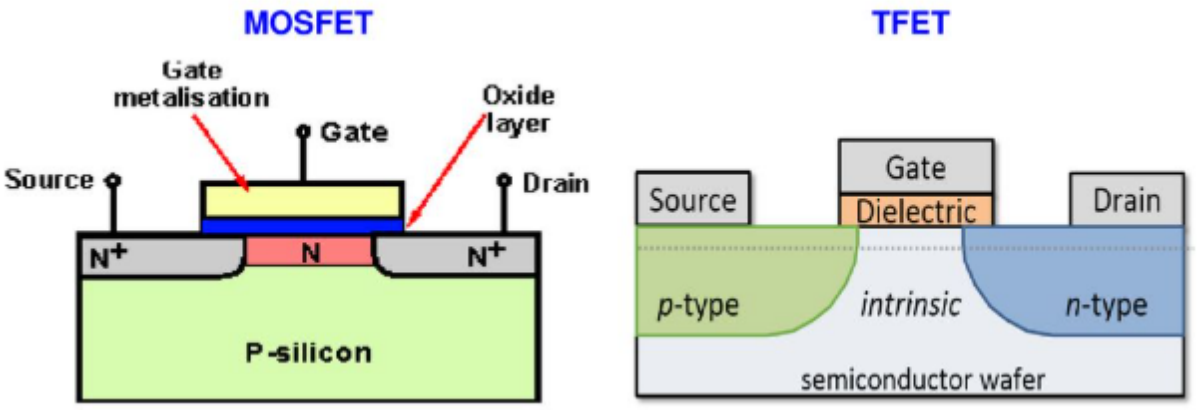


Figure 5 - Difference between Conventional MOSFET and TFET

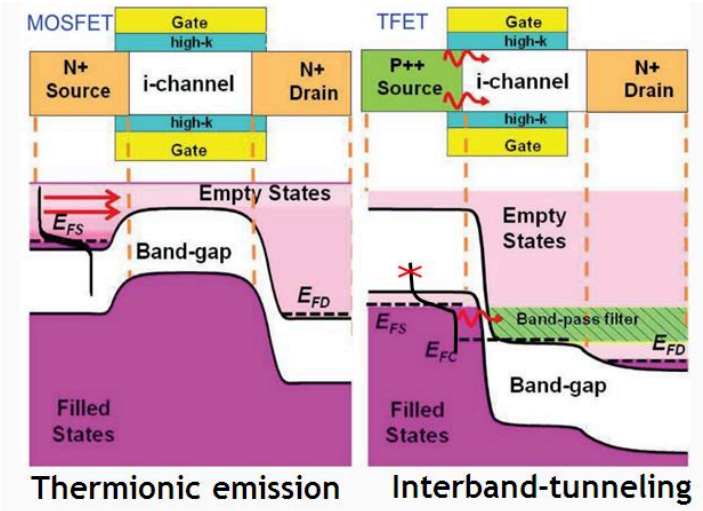


Figure 6 - Difference between thermionic emission and Quantum band-to-band tunnelling

Another critical parameter is the energy per decade switching (Subthreshold Swing), which is the energy used to change the drain current by one order of magnitude. For MOSFET, this value is thermally limited and typically above 60mV/decade, while

ISSN: 3061-9807

experimental TFET can achieve switches as low as 20-30mV/decade, significantly reducing the power consumption. The reciprocal of the slope of the log(Ids) vs. Vgs characteristic is defined as the subthreshold slope, S, and is one of the most critical performance metrics for FET in logic applications. It is highly desirable to have S as small as possible since this is the parameter that determines the amount of voltage swing necessary to switch a MOSFET from its "off" state to its "on" state.

SSmin, is the gate voltage necessary to change the drain current by one decade in MOSFET is given by

$$SS_{min} = \frac{k_b T}{e} ln(10) = 60\, mV/dec$$

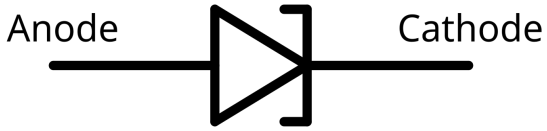
TFET operate based on band-to-band tunneling rather than thermionic emission, thus their SS behaves differently.

$$SS_T = \frac{2\sqrt{2} ln(10) \hbar}{-q\pi \sqrt{m_T E_g} \frac{dW_T}{d\Delta E}}$$

To ensure significant band-to-band tunnelling, the TFET structure must achieve an ultra-thin tunnelling barrier at the source-channel junction. The effective tunnelling width—defined as the physical thickness of the potential barrier through which carriers must tunnel—plays a critical role in determining the on-state current and switching characteristics. In this work, we considered device architectures and material systems that support tunnelling widths in the range of 1 to 3 nm, which is supported by previous modelling and experimental studies (Seabaugh & Zhang, 2010). By leveraging steep doping gradients, narrow bandgap semiconductors (such as InAs or Ge), and high gate electric fields, the tunnelling region can be compressed to sub-2 nm scales. This reduced barrier width significantly enhances the quantum tunnelling probability, following (5).

ISSN: 3061-9807

Figure 5: The circuit symbol for a tunnel diode



Another application of quantum tunnelling is tunnel diodes. These have a p-n junction that is incredibly narrow, allowing electrons to tunnel through it. The p-n junction is where the two semiconducting sides meet within the diode. On the "n" or negative side, with current flowing from the cathode, the material is doped (with intentional impurities) to produce free-moving electrons while the "p" or positive side is doped so the material has free moving electron *holes* - locations in an atom's structure when an electron is missing. In an ordinary diode, this allows the current to flow in only one direction when the incoming electrons "fill" the electron "holes".

The tunnel diode's incredibly narrow p-n junction (around $10\ nm$) allows electrons to tunnel through it. In forward bias operation, while potential difference rises, electrons tunnel through the barrier and fill valence states in the N-side of the junction, which in turn align with the electron holes of the P-side. This allows a current to flow across the junction. As voltage increases, these states become further misaligned and current decreases again. Therefore, we can call this "negative differential resistance" as current drops as voltage increases. This is the most useful aspect of tunnel diodes, as they can be thought of, for a period, as having negative resistance. Once the voltage increases above a certain threshold, it behaves as a regular diode, where electrons

ISSN: 3061-9807

conduct through the p-n junction, rather than tunnelling across it.

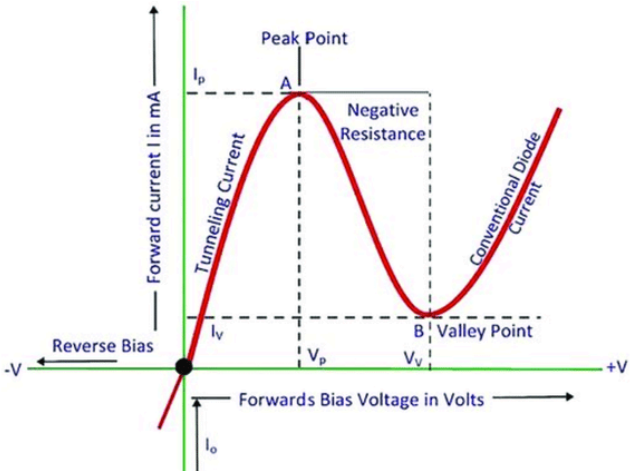


Figure 6: A graph showing the "negative resistance" region of the tunnel diode's I-V graph

Quantum tunnelling is also seen in Nuclear fusion. Nuclear fusion is the process where two light atomic nuclei combine to form a heavier nucleus, releasing significant amounts of energy. This reaction occurs naturally in stars, where immense pressure and temperature allow hydrogen nuclei to overcome their mutual electro-static repulsion (Coulomb barrier) and fuse.

However, under the conditions present in many fusion experiments on Earth, the kinetic energy of particles is often insufficient to overcome this Coulomb barrier. Quantum tunneling provides a probabilistic mechanism by which nuclei can penetrate this barrier, allowing fusion to occur at lower-than-classical expected energies.

1.2 Mathematical Description of Quantum Tunneling in Fusion

To model quantum tunneling in nuclear fusion, we analyze a one-dimensional potential barrier representing the Coulomb repulsion between two nuclei. The Schrödinger equation governs the behavior of a particle (in this case, a nucleus) approaching the potential barrier:

$$\frac{\hbar^2 d^2\psi(x)}{-2\mu\ dx^2} + v(x)\psi(x) = E\psi(x)$$

ISSN: 3061-9807

The Coulomb barrier is given by:

$$V(r) = \frac{Z_1 Z_2 e_2}{4\pi\epsilon_0 r}$$

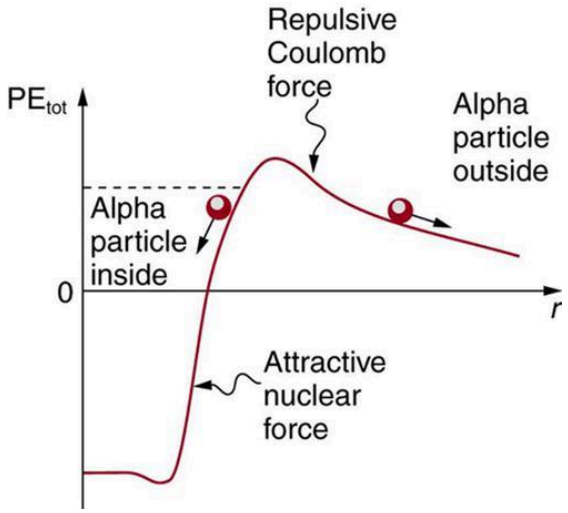
where Z1 and Z2 are the atomic numbers of the nuclei, e is the elementary charge, and **ϵ**0 is the vacuum permittivity.

The probability of tunneling through the barrier (Gamow factor) is given approximately

by:

$$2r2 \; P \approx exp \; - \; 2\mu(V\,(r) \; - \; E)\, dr(3)\hbar r1$$

This integral is evaluated between the classical turning points r1 and r2 where V (r) = E.



1.3 Application in Fusion Reactors

In devices such as tokamaks and stellarators, external magnetic fields confine high-temperature plasmas to replicate fusion conditions. At temperatures around 108 K, nuclei gain enough energy to approach each other closely, and quantum tunneling allows for fusion to occur even when classical mechanics predicts repulsion.

ISSN: 3061-9807

The fusion cross-section, which incorporates the tunneling probability, determines the reaction rate:

$$\sigma v \propto \infty 0\sigma(E)vf(E)\,dE$$

Where f(E) is the Maxwell-Boltzmann distribution of particle energies and σ(E) includes the tunneling probability.

3. Results

3.1 Results - STM microscope

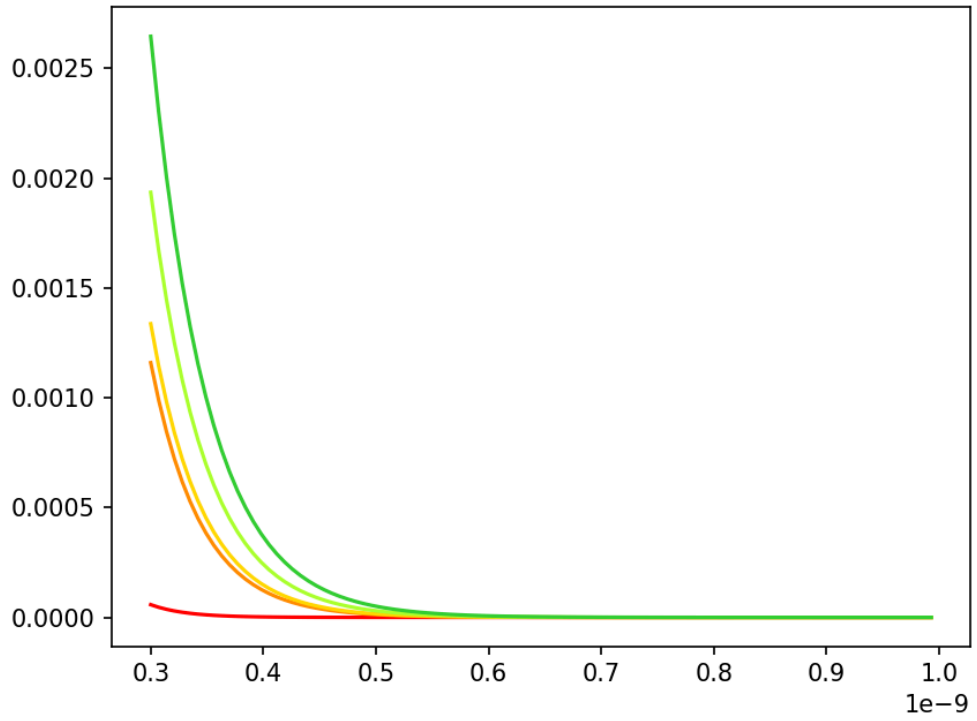


Figure 6 - Tunneling current against distance

The graph depicts the relationship between the detected current against the distance between the probe and the surface of the material. In the figure above, the curves (from bottom to top) each represent diamond, tungsten, graphite, silicon and zinc oxide, with a decreasing work function, i.e., in the order of descending potential barrier. Theoretically, the curve that is lower has a greater absolute value of gradient, therefore, more

ISSN: 3061-9807

sensitive. However, in the common distance range (0.3 to 1.0 nanometers), diamond would give negligible tunneling probability, as shown on the figure, it barely exceeds 0.0001 amps.

3.2 Results - Nanocapacitors

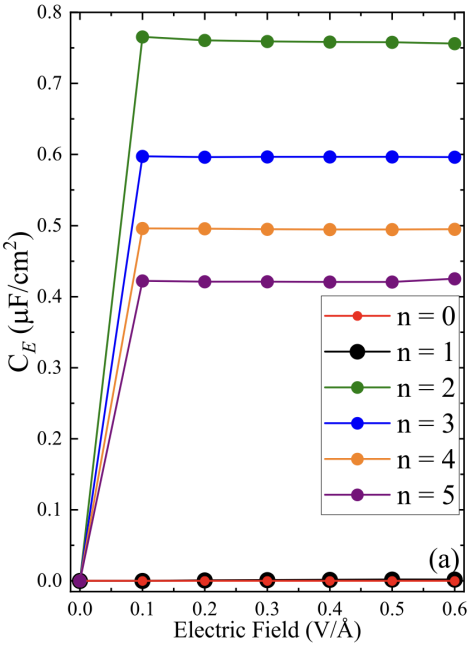
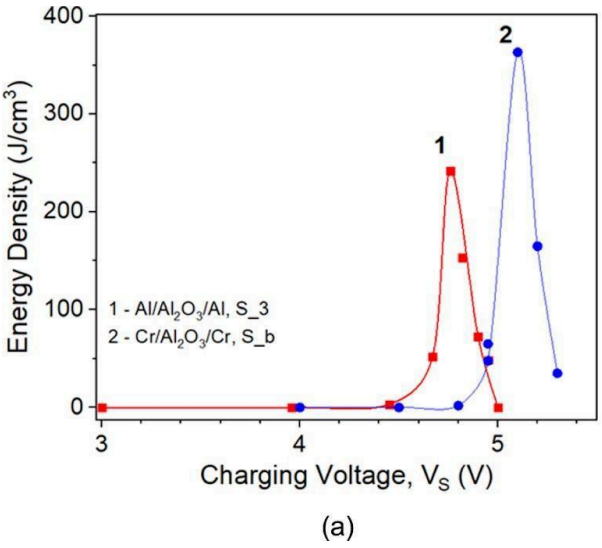


Figure 1 - the capacitance as a function of applied electric field of a dielectric nanocapacitor with borophene electrodes separated by insulating hexagonal boron nitride layers. Shown for number of layers “n = 1 - 5” [2]



ISSN: 3061-9807

Figure 2 showing the energy density in the nanolayer dielectric depending on the voltage applied during the charging process, shown for different samples with differing electrode materials. [3]

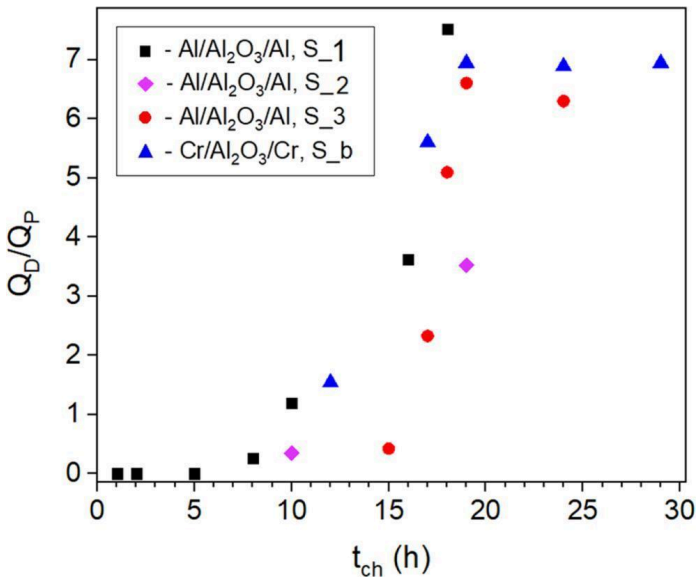


Figure 3 showing the charge stored in the dielectric, Q_D as a proportion of the charge stored in the electrodes, as a function of charging time, shown for different samples of capacitors [3]

ISSN: 3061-9807

3.3 Results - Tunnel Field-Effect Transistor (TFET)

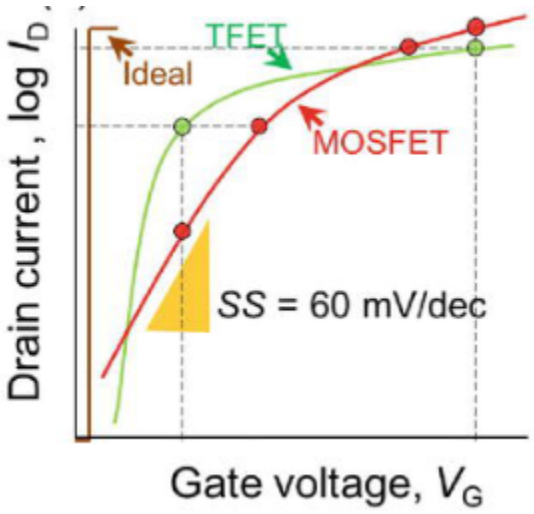


Figure 7 shows qualitative comparison of the SS of MOSFET and TFET. TFET (green), which has a steep off-on transition and a lower I_{OFF}. At low VG, because of the subthermionic SS, the TFET offers better performance and power reduction. At high VG, the MOSFET switch becomes a better solution for higher performance, thanks to the higher I_{ON}.

4. Discussion

4.1 Discussion - STM microscope

The sensitivity is the steepness of the curve in Figure 6, i.e., $\frac{dI}{dd}$, in other words, the greater the difference in current detected by the probe with fixed change in distance, the greater resolution the microscope will have. Theoretically the greater the work function of the material, the more sensitive it would be, but the reality is quite counter-intuitive, those with middle-low work function show greater sensitivity within the realistic range of distances. In fact, mathematically speaking, the steepness should be greater for diamonds, however, it has such a large work function, that the probability of tunneling approaches 0, the theoretical sensitiveness can only be achieved when the probe is 0.05 or less nanometers away from the surface of the observed material, which is highly

difficult to control and not practical. Similarly, the steepest part of the curve of those with high work function usually comes before $0.3nm$, which is excluded from the domain of the graph, just like in the diamond's case. Thus, there are some limitations of the material that can be observed by the STM. The most ideal material to observe is tungsten, or graphite.

4.2 Discussion - Nanocapacitors

Figure 1 shows that capacitance does not increase from 0 when there is only a boron nitride monolayer as the electrodes are short circuited, however the maximum capacitance is achieved when n = 2, and it decreases as n increases as the electrodes get further away, demonstrating the benefits of using nanocapacitors in electronic components.

Figure 2 shows a sharp peak in energy density at a certain charging voltage. This is because as the strength of the electric field increases, electrons become more likely to tunnel through the metal surface and can tunnel further into the dielectric layer. This means that as the voltage increases more electron traps in the dielectric can be filled meaning more energy can be stored, however if this becomes too large electrons can tunnel into too much of the dielectric, removing the asymmetrical charge distribution, causing a lower discharge current and lower energy storage. At this peak voltage, electrons can tunnel only into the region of the dielectric layer near the anode. However, the maximum energy density achieved is higher than the highest managed without this technique in other nanocapacitors, achieving similar values to alkaline batteries, demonstrating the large impact of this discovery.

Figure 3 shows that the charging of the dielectric can take a very long time, with some samples taking up to 20 hours of charging to reach saturation. This demonstrates the capacitor having similar properties to a conventional battery, with far longer charging times than regular capacitors. However, the charge stored in the dielectric can be more than 7 times greater than the charge in the electrodes, and can be stored stably provided the temperature remains low enough. This charge can be released when the temperature is increased, providing a potentially environmentally friendly method of energy storage that could be a valuable alternative to electrochemical storage systems.

4.3 Discussion - Tunnel Field-Effect Transistor (TFET)

ISSN: 3061-9807

TFET has many advantages that make it attractive to produce low-power and high-efficiency electronics. The ability to switch on gate voltage below the thermal limit of 60mV/decade enables them to operate at lower supply voltages, as a result power consumption is reduced. In addition, it has low off-state leakage as when the gate is off, the energy bands are far apart from each other, thus quantum tunnelling is restricted. There will be no thermionic emission occurrence in TFET that might cause battery drain and more static power consumption as compared to MOSFET. This is because in MOSFET, even if the gate voltage is below threshold, some electrons still gain enough thermal energy to cross the barrier, and as the gate oxide gets thinner in modern chips, electrons can tunnel through the gate insulator, causing leakage.

However, there are also some limitations for TFET which require further research. First, it is low on current. While TFETs have low off-state leakage, their on-state current is lower than MOSFET, which limits their speed. Furthermore, small tunnelling distances make their behaviour more sensitive and more challenging to manufacturing variations and processes.

5. Conclusions

Quantum Tunnelling has many different uses ranging far beyond what is discussed in this report, but we have shown a variety of applications, some which are theoretically proven and still being researched and some which are in common use. The Scanning Tunnelling Microscope was one of the first uses of quantum tunnelling following many theoretical discoveries throughout the 20th century, showing how the phenomenon can be applied to give highly sensitive images of material surfaces. Additionally, quantum tunnelling has wide-reaching effects in electronics, where the constant effort of miniaturisation is limited due to quantum tunnelling effects, such as in nanocapacitors. However, it is also a key phenomenon in the functioning of semiconductors, with applications in tunnel diodes and TFET transistors, as well as being important in flash memory. Quantum tunnelling is also at the forefront of research, especially relating to electronics, and the experimental results of its use in nanocapacitors could have a large impact on future solutions for energy storage, although it is still in an early stage and there are significant drawbacks. Lastly, since its discovery, Quantum tunnelling has been found to explain other phenomena we see such as nuclear fusion, showing how important it is for increasing physical understanding. This report has shown the importance of Quantum tunnelling in

ISSN: 3061-9807

different areas of physics, which will continue to increase as more research is continued to be done into its future uses.

ISSN: 3061-9807

Bibliography

[1] Lauren C. Haspert, Sang Bok Lee, Gary W. Rubloff (2012-3-06).“Nanoengineering Strategies for Metal-Insulator-Metal Electrostatic Nanocapacitors”

[2] Y. Mogulkoc ,A. Mogulkoc , H. E. Guler, E. Durgun (2021-12-13) “Design of nanoscale capacitors based on metallic borophene and insulating boron nitride layers”

[3] Eduard Ilin, Irina Burkova, Eugene V Colla, Michael Pak, Alexey Bezryadin (2021-01-25). “Giant energy storage effect in nanolayer capacitors charged by the field emission tunneling”

[4] Fowler, R.H.; Dr. L. Nordheim (1928-05-01). "Electron Emission in Intense Electric Fields"

D. Berard, (2017) “Home Built STM”, available at https://dberard.com/

Koonin, S. E., & Nauenberg, M. (1981). *Quantum tunneling and nuclear fusion*. Nature, 289(5799), 393–394. https://doi.org/10.1038/289393a0

Rolfs, C. E., & Rodney, W. S. (1988). *Cauldrons in the Cosmos: Nuclear Astrophysics*. University of Chicago Press.

Zhao, W., & Gong, Z. (2020). *Quantum tunneling effect and its significance in nuclear fusion and fission processes*. Journal of Modern Physics, 11(2), 147–159.

O'Shea, B. (2022). *Quantum tunneling and its impact on fusion ignition in stars and laboratories*. Nature Reviews Physics, 4(5), 340–354.

Fischer, F. R., & Liljeroth, P. (2020). *Scanning tunneling microscopy: From atoms to molecules*. Nature Reviews Chemistry, 4(5), 386–403.

Wiesendanger, R. (2021). *Spin mapping at the atomic scale by STM*. Nature Reviews Physics, 3(1), 39–50.

Mogulkoc, Y., Mogulkoc, A., Guler, H. E., & Durgun, E. (2021). *Design of nanoscale capacitors based on metallic borophene and insulating boron nitride layers*. Scientific Reports, 11(1), 23598.

Wu, C., Wang, Z., Xiao, Y., & Li, Y. (2021). *High-performance 2D material-based nanocapacitors for energy storage applications*. Advanced Functional Materials, 31(25), 2101352.

"Gravitational Lensing"

Authors: Sophie Allen, Anthony Ge, Zac Lightman, Elva Wang

Research Mentors: Nikita Azevedo, Toby Bhanji

ISSN: 3061-9807

Abstract

According to Einstein's theory of General Relativity, massive objects distort spacetime around them. This curvature of spacetime bends the trajectories of light from distant sources, a phenomenon known as gravitational lensing. This paper outlines the theoretical foundations of lensing, including the Shapiro time delay, the derivation of the deflection angle, and the lens equation. We also discuss observational techniques, from strong lensing (e.g. Einstein rings) to weak lensing (statistical analysis to map dark-matter distributions), and highlight landmark discoveries such as the 1919 eclipse that validates Einstein's theory of GR. We discuss the effects of microlensing, a method used to detect the dark matter candidate called MACHOs. Finally, we dive into an exciting observational study of LRDs (Little Red Dots), observed differently by Hubble and JWST, and discuss what the spectra could mean theoretically.

1. Time delay and time dilation

Shapiro Time delay is the phenomenon in which light slows down as it travels through a gravitational field. The equation for the one-way Shapiro time delay is [1]:

$$T_{\text{sh}} = -\frac{2GM}{c^3} \ln(1 - \vec{R} \cdot \vec{x}) \tag{1}$$

Where $\vec{R}$ is the vector from Earth to the lensed object and $\vec{x}$ is the vector from Earth to the massive object.

Time is not uniform in the universe. According to Einstein's theory of General Relativity, time is influenced by energy and mass, which curve spacetime. Gravitational Time Dilation causes time to slow down in regions of stronger gravity. Starting with the Schwarzschild metric, which describes how to calculate distances and time intervals in curved spacetime, this becomes apparent. The metric is as follows [2]:

$$ds^2 = -\left(1 - \frac{2GM}{r}\right) c^2 dt^2 + \left(1 - \frac{2GM}{r}\right)^{-1} dr^2 + r^2 d\theta^2 + r^2 \sin^2\theta \, d\phi^2 \tag{2}$$

Let there be a stationary bystander who is observing in spacetime. Thus $d\theta = dr = d\phi = 0$. So the metric becomes $ds^2 = -(1 - \frac{2GM}{r})dt^2$. Plugging in $d\tau^2 = ds^2$ (where $d\tau$ represents the proper time of the bystander) This yields $d\tau = dt\sqrt{1 - \frac{2GM}{r}}$ [3]. This relates the proper time of the bystander ($d\tau$) to time somewhere far away (dt). This means $d\tau < dt$ and time moves more slowly near a large mass.

Additionally, we can use the time delay to find Hubble's constant H_0, the current rate of expansion of the universe. The equation $\Delta t \propto \frac{D_{\Delta t}}{c} \Delta\phi$ relates the time delay (Δt) to Hubble's Constant where $D_{\Delta t}$ is the time-delay distance and $D_{\Delta t} \propto \frac{1}{H_0}$. Rearranging yields $H_0 \propto \frac{1}{D_{\Delta t}}$ where H_0 can be calculated after the time-delay distance is calculated from the images.

ISSN: 3061-9807

2. The deflection angle

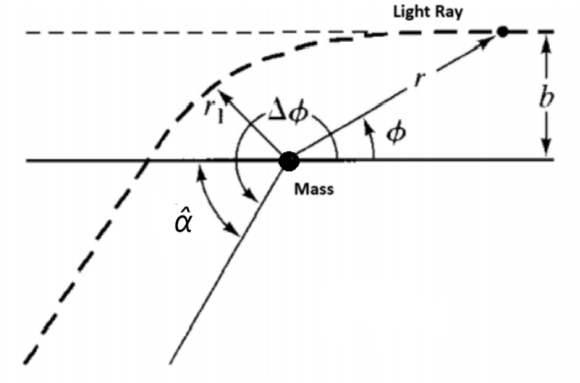


Figure 1: Diagram of the deflection of light

The deflection angle $\hat{\alpha}$ (Figure 1) is the total angle by which the trajectory of light is bent as it passes near a massive object, such as a black hole. Here, we present the derivation (Hartle, Chapter 9 [2]) that uses the curvature of spacetime around an ideal Schwarzchild black hole described by this metric (in c = G = 1 units):

$$ds^2 = -\left(1 - \frac{2M}{r}\right) dt^2 + \left(1 - \frac{2M}{r}\right)^{-1} dr^2 + r^2(d\theta^2 + \sin^2\theta\, d\phi^2) \tag{3}$$

Since the orbit of the light ray is in the equatorial plane, we can set $\theta = \pi/2$. Light follows null geodesic ($ds^2 = 0$), so the metric simplifies to:

$$-\left(1 - \frac{2M}{r}\right) dt^2 + \left(1 - \frac{2M}{r}\right)^{-1} dr^2 + r^2 d\phi^2 = 0. \tag{4}$$

According to Hartle, these quantities are conserved (λ is an affine parameter):

$$\begin{aligned} e &\equiv -\xi \cdot u = \left(1 - \frac{2M}{r}\right) \frac{dt}{d\lambda}, \\ \ell &\equiv \eta \cdot u = r^2 \sin^2\theta\, \frac{d\phi}{d\lambda}, \end{aligned} \tag{5}$$

Substitute

$$\frac{dt}{d\lambda} = \frac{e}{1 - 2M/r} \quad \text{and} \quad \frac{d\phi}{d\lambda} = \frac{\ell}{r^2} \tag{6}$$

into $ds^2 = 0$:

$$-\frac{e^2}{\left(1 - \frac{2M}{r}\right)} + \left(1 - \frac{2M}{r}\right)^{-1} \left(\frac{dr}{d\lambda}\right)^2 + \frac{\ell^2}{r^2} = 0. \tag{7}$$

and rearrange to get:

$$\left(\frac{dr}{d\lambda}\right)^2 = e^2 - \frac{\ell^2}{r^2}\left(1 - \frac{2M}{r}\right) \tag{8}$$

ISSN: 3061-9807

Then, we define an impact parameter $b = |\ell/e|$ which is the closest approach of the light ray to the massive object. We consider a light ray approaching the massive object in the direction parallel to the x-axis at a distance d away from it [4]. For a source of light far enough away ($r \to \infty$, $r \gg 2M$), b approximates to d.

The orbital equation of the light ray becomes:

$$\frac{d\phi}{dr} = \frac{d\phi/d\lambda}{dr/d\lambda} = \frac{\ell/r^2}{\sqrt{e^2 - \frac{\ell^2}{r^2}\left(1 - \frac{2M}{r}\right)}} = \frac{1}{r^2}\left[\frac{1}{b^2} - \frac{1}{r^2}\left(1 - \frac{2M}{r}\right)\right]^{-1/2}. \tag{9}$$

To find the total angle swept by the light ray's trajectory, we integrate this expression. Note that the total angle $\Delta\phi$ swept equals twice the angle swept from infinity to the turning point $r = r_1$ (where $dr/d\lambda = 0$, as shown in Figure 1):

$$\Delta\phi = 2\int_{r_1}^{\infty} \frac{dr}{r^2}\left[\frac{1}{b^2} - \frac{1}{r^2}\left(1 - \frac{2M}{r}\right)\right]^{-1/2}. \tag{10}$$

This evaluates to:

$$\Delta\phi \approx \pi + \frac{4M}{b}. \tag{11}$$

As shown in Figure 1, the deflection angle is:

$$\hat{\alpha} = \Delta\phi - \pi = \frac{4M}{b} \tag{12}$$

Restoring G and c:

$$\boxed{\hat{\alpha} = \frac{4GM}{c^2 b}} \tag{13}$$

In 1804, Soldner first calculated the deflection angle of light as $2GM/c^2b$ by treating light as a Newtonian particle moving at speed c. However, in 1916, Einstein's general relativity predicted a deflection angle twice this value (which was the same as the expression above)[5]. For light grazing the Sun (see Figure 2), these theories predicted 0.8 arcseconds (Newtonian) and 1.7 arcseconds (GR), respectively. Subsequent observations of the 1919 solar eclipse confirmed Einstein's prediction.

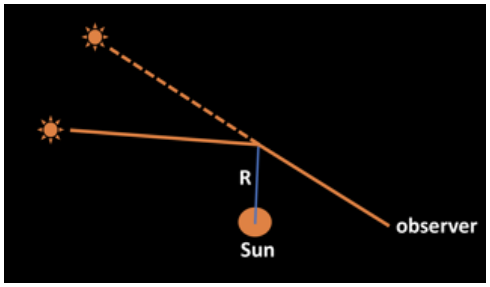


Figure 2: Deflection by the sun [6]

3. Lens equation

A simple geometric model for a standard gravitational lens and a source is summarized in Figure 3 below:

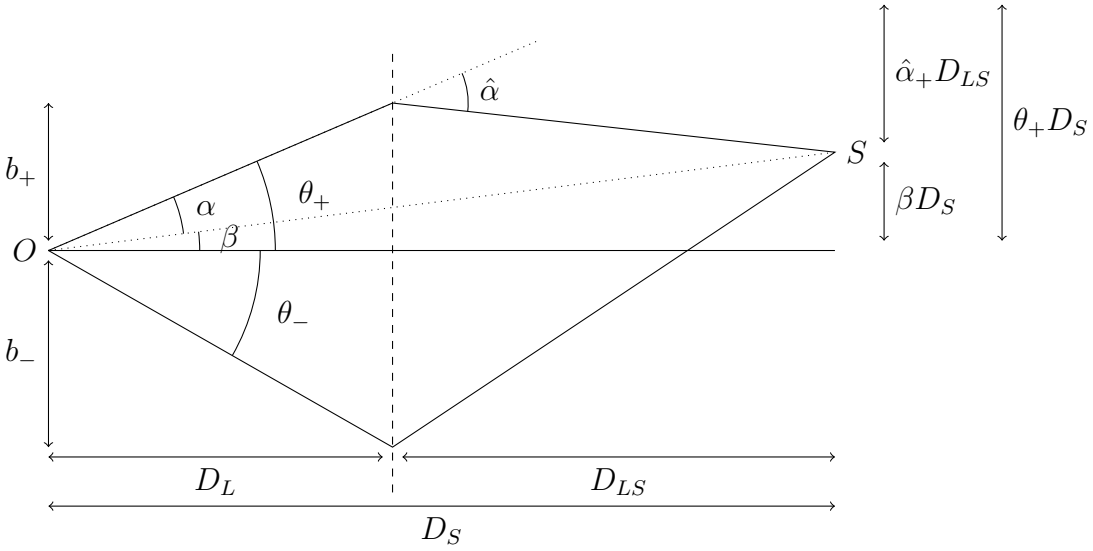


Figure 3: Cross-section showing light rays travelling from source S to observer O

We use the thin lens approximation, where the lens is treated as a point and all deflection takes place in a transverse plane at that point. The angles involved are small, so we can treat triangles as sectors of a circle. We arrive at the lens equation [2][7]:

$$\begin{aligned} \theta D_s &= \beta D_S + \hat{\alpha} D_{LS} \\ \beta &= \theta - \frac{D_{LS}}{D_S}\hat{\alpha} \end{aligned} \tag{14}$$

This relates the real position of the source to the observed position assuming light travels through a single gravitational field. Note that in relativity, D_{LS} is not always equivalent to $D_S - D_L$. We arrive at the vector form:

$$\vec{\beta} = \vec{\theta} - \frac{D_{LS}}{D_S}\vec{\hat{\alpha}} \tag{15}$$

Where $\vec{\beta}$ would be the vector angle to the source if no lensing had occurred and $\vec{\theta}$ is the vector angle to the lensed image [8]. Furthermore, if we define the reduced deflection angle $\vec{\alpha} \equiv \frac{D_{LS}}{D_S}\vec{\hat{\alpha}}$ then we obtain:

$$\vec{\beta} = \vec{\theta} - \vec{\alpha} \tag{16}$$

Additionally, using $b \approx \theta D_L$ we obtain $\hat{\alpha} = \frac{4GM}{c^2 b} = \frac{4GM}{c^2 \theta D_L}$ [9]. As previously derived, $\beta = \theta - \frac{D_{LS}}{D_S}\hat{\alpha}$. Substituting $\hat{\alpha}$ obtains:

$$\begin{aligned} \beta &= \theta - \frac{D_{LS}}{D_S}\frac{4GM}{c^2 \theta D_L} \\ \theta(\theta - \beta) &= \frac{4GM}{c^2}\frac{D_{LS}}{D_L D_S} \end{aligned} \tag{17}$$

We define θ_E to be the value of θ at which $\beta = 0$. Here there is perfect alignment of the source, lens and observer. Therefore [10]:

$$\theta_E^2 = \frac{4GM}{c^2}\frac{D_{LS}}{D_L D_S} \tag{18}$$

$$\beta = \theta - \frac{\theta_E^2}{\theta} \tag{19}$$

This interpretation of the lens equation is essential for image positioning, as θ determines the apparent angular position of the images after lensing. Note that the deflection angle for a black hole can be simplified, since the Schwarzschild radius is given by $r_s = \frac{2Gm}{c^2}$, while the escape velocity $v_e = \sqrt{\frac{2Gm}{r}} = \beta_e c$, evaluating to a fraction of the speed of light. Consequently, we can express the deflection angle as [9]:

$$\hat{\alpha} = 2\frac{r_s}{r} = 2(\frac{v_e}{c})^2 = 2\beta_e^2 \tag{20}$$

Gravitational lensing cannot be considered with an ordinary geometric optic equation linear object-distance relations cannot be assumed; the lensing depends on the curvature of spacetime and matter distribution. Light therefore follows geodesics due to spacetime curvature caused by the lens.

$$\frac{d^2x^\mu}{d\tau^2} + \Gamma^\mu_{\nu\lambda}\frac{dx^\nu}{d\tau}\frac{dx^\lambda}{d\tau} = 0 \tag{21}$$

Here, $\frac{d^2x^\mu}{d\tau^2}$ is the acceleration of a particle with respect to proper time, $\Gamma^\mu_{\nu\lambda}$ is a Christoffel symbol with affine parameter μ, and $\frac{dx^\nu}{d\tau}\frac{dx^\lambda}{d\tau}$ is the tangent vector to the particle's geodesic. [11]

4.Surface mass density

Suppose an observer looks towards a lensing object in the sky. The spherical object appears as a circle. The amount of mass in each unit area of the projection of the sphere onto a circle is given by Σ, the surface mass density. The surface mass density at a point on the circle is equal to the sum of the mass in each thin column extending from the observer to the circle. Hence we have [10]:

$$\Sigma(b) = \int_0^{D_s} \rho(b, z)dz \tag{22}$$

The mass of the lens is the sum of the masses of concentric rings of thickness db' from the centre of the lens:

$$M(b) = \int_0^b \Sigma(b')(2\pi b')db' = 2\pi\int_0^b \Sigma(b')b'db' \tag{23}$$

Assuming constant surface mass density:

$$\hat{\alpha} = \frac{4GM}{c^2 b} = \frac{4G}{c^2}\frac{2\pi\int_0^b b'db'\Sigma}{b} = \frac{4G\pi b\Sigma}{c^2} \quad \text{so} \quad \Sigma = \frac{c^2\hat{\alpha}}{4G\pi b} = \frac{c^2\alpha}{4G\pi}\frac{D_S}{\theta D_L D_{LS}} \tag{24}$$

The critical density occurs when $\beta = 0$ so $\alpha = \theta$ giving:

ISSN: 3061-9807

$$\Sigma_{cr} = \frac{c^2}{4G\pi}\frac{D_S}{D_L D_{LS}} \quad (25) \qquad \alpha = \frac{\Sigma}{\Sigma_{cr}}\theta = \kappa\theta \quad (26)$$

The convergence $\kappa = \frac{\Sigma}{\Sigma_{cr}}$, and strong lensing occurs when $\Sigma > \Sigma_{cr}$.

5. Multiple images

From earlier we have that $\theta(\theta - \beta) = \frac{4GM}{c^2}\frac{D_{LS}}{D_L D_S}$. A situation with perfect alignment between the source, lensing object and observer occurs when $\beta = 0$, which makes Figure 3 symmetric in the horizontal axis so $\theta_+ = \theta_E = \theta_- = \frac{4GM}{c^2}\frac{D_{LS}}{D_L D_S \theta_+}$. Hence:

$$\theta_E = \sqrt{\frac{4GM}{c^2}\frac{D_{LS}}{D_L D_S}} \quad (27)$$

Since we have perfect alignment, a ring of light will form around the massive object with angular radius θ_E, the Einstein radius. Otherwise we still have $\beta = \theta - \frac{\theta_E^2}{\theta}$ so:

$$\theta_\pm = \frac{1}{2}(\beta \pm \sqrt{\beta^2 + 4\theta_E^2}) \quad (28)$$

These represent the angular positions in which the two lensed images form. The overall image could be an elliptical ring, or multiple distorted images rather than a continuous shape. Additionally an image will only form if $\kappa > 1$. The number of images produced will always be odd according to odd number theorem [12], though since this includes the central, original image, it can also be thought of as additional images appearing in pairs.

6. Brightness

Gravitational lensing can magnifies objects. Flux is conserved, but the observed area increases, so total brightness increases. Consider a system of concentric rings of thickness $d\beta$ and $d\theta$ forming the unmagnified image and the image we perceive respectively, where θ could be θ_+ or θ_-. Therefore brightness magnification μ is [10]:

$$\mu = \frac{\text{Image size}}{\text{Actual size}} = \frac{2\pi\theta \cdot d\theta}{2\pi\beta \cdot d\beta} = \frac{\theta}{\beta}\frac{d\theta}{d\beta} \quad (29)$$

Hence magnification due to $\theta_\pm$ is:

$$\mu_\pm = \left|\frac{\frac{1}{2}(\beta \pm \sqrt{\beta^2 + 4\theta_E^2})}{\beta}(\frac{1}{2} \pm \frac{1}{4}(\beta^2 + 4\theta_E^2)^{-\frac{1}{2}})\right| = \pm\frac{1}{2} + \frac{u^2+2}{2u\sqrt{u^2+4}} \quad (30)$$

Total magnification becomes:

$$\mu = \frac{u^2+2}{u\sqrt{u^2+4}} \quad (31)$$

Notably for a circular Einstein ring, when $\beta = 0$ we have $u = 0$ so magnification approaches infinity.

ISSN: 3061-9807

7. Lensing potential

We define lensing potential ψ as a projection of gravitational potential Φ onto the lens plane. We then define the gradient of the lensing potential to equal the reduced deflection angle α. This leads to the definition [13]:

$$\psi(\vec{\theta}) = \frac{D_{LS}}{D_L D_S}\frac{2}{c^2}\int \Phi(\vec{b}, z)dz \tag{32}$$

Using $b = \theta D_L$, the gradient becomes:

$$\vec{\nabla}_{\vec{\theta}}\psi = D_L\vec{\nabla}_{\vec{b}}\psi = D_L\frac{D_{LS}}{D_S D_L}\frac{2}{c^2}\int \vec{\nabla}_{\perp}\Phi dz = \vec{\alpha} \tag{33}$$

Additionally, using Poisson's equation for gravity, $\nabla^2\Phi = 4\pi G\rho$, we have that:

$$\nabla^2_{\theta}\phi = D_L\vec{\nabla}_b \cdot \frac{D_{LS}}{D_S}\frac{2}{c^2}\int \vec{\nabla}_b\Phi dz = \frac{D_L D_{LS}}{D_S}\frac{2}{c^2}\int \nabla^2_b\Phi = \frac{2\frac{4\pi G\Sigma}{c^2}\frac{D_L D_{LS}}{D_S}\theta}{\theta} = \frac{2\alpha}{\theta} = 2\kappa \tag{34}$$

8. Redshift

One alternative method to determining the Hubble constant is through using redshifts of distant gravitationally lensed galaxies. Let $a(t)$ be a scaling parameter of the universe that acts as the ratio between the size of the universe now and the size of the universe in the past. Using the FLRW metric [14]:

$$ds^2 = -dt^2 + a(t)^2(\frac{dr^2}{1 - Kr^2} + r^2\Omega) \tag{35}$$

where K is the curvature of the universe, it can be shown that:

$$\frac{a_0}{a_e} = z + 1 \tag{36}$$

Where z is the redshift of an observed object. Consider two points in time: t_0 (now) and t_e, the time at which a photon is released from the lensed object that is observed at t_0. We find using $\frac{dt_e}{dt_0} = \frac{da_e}{da_0}$:

$$\frac{dz}{dt_0} = \frac{1}{a_e}\frac{da_0}{dt_0} - \frac{a_0}{a_e^2}\frac{da_e}{dt_0} = \frac{a_0}{a_e}\frac{\dot{a_0}}{a_0} - \frac{\dot{a_e}}{a_e} = (z+1)H_0 - H(z) \tag{37}$$

We will now integrate redshift into the lens equation. Let $\chi_S, \chi_L, \chi_{LS}$ be co-moving distances. That is they are independent of the expansion of the universe. We define these variables such that $D_S = a_S\chi_S, D_L = a_L\chi_L$. In the general case of a co-moving distance, using $a = \frac{a_0}{1+z}$ and $\frac{da}{dz} = -\frac{a_0}{(1+z)^2}$ we find that [15]:

$$dt = -\frac{1}{H(z)}\frac{a_0}{(1+z)^2}dz\frac{1+z}{a_0} = -\frac{1}{H(z)}\frac{1}{1+z}dz \tag{38}$$

Therefore:

ISSN: 3061-9807

$$\chi = -\int_{t_e}^{t_0} \frac{c}{a} dt' = \frac{1}{a} \frac{1}{1+z_S} \int_0^{z_S} \frac{c}{H(z')} dz'$$
$$D_L = a_L \chi_L = \frac{1}{1+z_S} \int_0^{z_S} \frac{c}{H(z')} dz' \tag{39}$$

And D_S similarly. However since an observer at the lens sees a universe that is smaller by a factor of $\frac{1}{1+z_L}$:

$$D_{LS} = a_L \frac{a_S}{a_L} (\chi_S - \chi_L) = \frac{1}{1+z_S} \int_{z_L}^{z_S} \frac{c}{H(z')} dz' \tag{40}$$

Additionally, using the lens equation we have that:

$$\theta(\theta - \beta) = \theta_E^2 = \frac{4GM}{c^2} \frac{D_{LS}}{D_L D_S} = \frac{4GM}{c^2} (1+z_L)(\frac{1}{\chi_L} - \frac{1}{\chi_S}) \tag{41}$$

From this we see that the Einstein radius will change over time. This is because as the universe expands, D_L, D_S and D_{LS} will increase, whilst b does not. This also means that β is constant over time since it relies solely on D_S. Recalling that $\theta_\pm = \frac{1}{2}(\beta \pm \sqrt{\beta^2 + 4\theta_E^2}$ we obtain $\beta = \theta_+ + \theta_-$ and $\theta_E^2 = -\theta_+ \theta_-$. By first taking the derivative with respect to t_0 on both sides of $\theta_E^2 = -\theta_+ \theta_-$ it can be shown that:

$$\frac{2}{\theta_E} \frac{d\theta_E}{dt_0} = H_0 - \frac{H_L}{1+z_L} \tag{42}$$

We can also consider the time delay accounting for the expansion of the universe through:

$$\frac{1}{\Delta} \frac{d\Delta}{dt_0} = (H_0 - \frac{H_L}{1+z_L}) \frac{\ln \frac{-\theta_-}{\theta_+} + \frac{\theta_- + \theta_+}{\theta_- - \theta_+}}{\ln \frac{-\theta_-}{\theta_+} + \frac{\theta_+^2 + \theta_-^2}{\theta_+ \theta_-}} \tag{43}$$

where Δ = total time delay = $\Delta_{geom} + \Delta_{pot}$ However it should be worth noting that using this method to determine the Hubble constant would take an extremely long time to detect any changes.

9. Microlensing

Microlensing relies on relative motion between the lens and the source and produces a dynamic change in brightness rather than many static images. Examples of microlensers include MACHOS (Massive Compact Halo Objects), which is a candidate for dark matter, and difficult to detect using anything aside their occasional gravitational disruptions and involves astronomical objects like brown dwarfs and primordial black holes. Figure 4 shows an example of how the relativistic motion in the observer's line of sight affects the observation. Here the lens is occulting the source, but the light has bent around so the source can be seen[7].

The time taken for a MACHO to move one Einstein radius is [2]:

$$t = \frac{\theta_E D_L}{\nu} \tag{44}$$

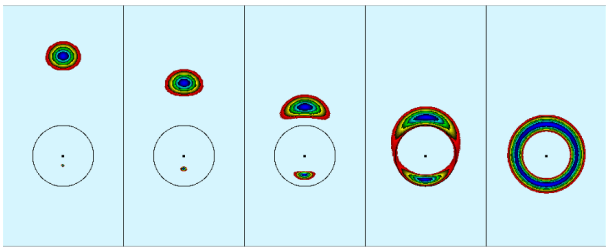


Figure 4: The alignment between lens and source gets better, until it is perfect in the rightmost panel. This observation is called an Einstein ring

where ν is the MACHO velocity. As the MACHO aligns with the observer's line of sight and the lens, the apparent brightness of the source increases by the amplification factor $A(u) = \frac{u^2+2}{u\sqrt{u^2+4}}$. The change in observed brightness can be plotted on a light curve.

Imaging also helps to plot critical and caustic curves, which allow astronomers to predict observations as the MACHO moves through the Einstein radius [16]. Critical curves show where the image will be infinitely magnified. Caustic curves show where there will be multiple images from the same source. Critical curves are determined by taking a set of x values, then calculating the determinant of the Jacobian matrix $\hat{A}$. A Jacobian is a matrix transformation that approximates non-linear transformations as linear ones at a local level. Let $\hat{A}$ be the Jacobian of the lens equation $\vec{\beta} = \vec{\theta} - \vec{\alpha}(\vec{\theta})$. Then [17]

$$\hat{A}_{ij} = \frac{\partial \vec{\beta_i}}{\partial \vec{\theta_j}} = (\delta_{ij} - \frac{\partial \vec{\alpha_i}}{\partial \vec{\theta_j}}) = (\delta_{ij} - \frac{\partial^2 \psi}{\partial \vec{\theta_i} \partial \vec{\theta_j}}) \tag{45}$$

Additionally, we know that locally, transformations will have a magnification component and a shear component. The shear component is to better approximate the more elliptical shape of lensed objects, and the magnification we have already shown. We will obtain a 2x2 matrix, noting that $\hat{A}_{12} = \hat{A}_{21}$ We recall from Section 7 that:

$$\kappa = \frac{1}{2}\nabla^2_{\vec{\theta}}\psi = \frac{1}{2}(\frac{\partial^2 \psi}{\partial \vec{\theta_1^2}} + \frac{\partial^2 \psi}{\partial \vec{\theta_2^2}}) \tag{46}$$

Let

$$\begin{aligned} \gamma_1(\vec{\theta}) &= \frac{1}{2}(\frac{\partial^2 \psi}{\partial \vec{\theta_1^2}} - \frac{\partial^2 \psi}{\partial \vec{\theta_2^2}}) = \gamma \cos(2\phi(\vec{\theta})) \qquad \gamma_2(\vec{\theta}) = \frac{\partial^2 \psi}{\partial \vec{\theta_1}\vec{\theta_2}} = \gamma \sin(2\phi(\vec{\theta})) \\ \gamma(\vec{\theta}) &= \sqrt{\gamma_1^2 + \gamma_2^2} \qquad\qquad\qquad\qquad \phi = \arctan(\frac{\gamma_2}{\gamma_1}) \end{aligned} \tag{47}$$

The Jacobian matrix then becomes:

$$\begin{aligned} \hat{A} &= \begin{pmatrix} 1 - \frac{\partial^2 \psi}{\partial \vec{\theta_1^2}} & -\frac{\partial^2 \psi}{\partial \vec{\theta_1}\vec{\theta_2}} \\ -\frac{\partial^2 \psi}{\partial \vec{\theta_1}\vec{\theta_2}} & 1 - \frac{\partial^2 \psi}{\partial \vec{\theta_2^2}} \end{pmatrix} = \begin{pmatrix} 1 - \kappa - \gamma_1 & -\gamma_2 \\ -\gamma_2 & 1 - \kappa + \gamma_1 \end{pmatrix} \\ &= (1-\kappa)\begin{pmatrix} 1 & 0 \\ 0 & 1 \end{pmatrix} - \gamma \begin{pmatrix} \cos(2\phi) & \sin(2\phi) \\ \sin(2\phi) & -\cos(2\phi) \end{pmatrix} \end{aligned} \tag{48}$$

ISSN: 3061-9807

Additionally, since we are mapping β onto θ, the determinant of the matrix encodes the change in area and therefore brightness: [18]:

$$\mu = \frac{1}{|\hat{A}|} = \frac{1}{(1-\kappa)^2 - \gamma^2} \tag{49}$$

If $|\hat{A}| = 0$, then the image has been infinitely magnified, and a critical curve should be plotted. If the tangential eigenvalue associated with distortion perpendicular to the radial plane evaluates to 0, or $\lambda_t = 1 - \kappa - \gamma = 0$ then a tangential critical curve should be plotted. If the radial eigenvalue associated with distortion along the radial plane evaluates to 0, or $\lambda_r = 1 - \kappa + \gamma$ then a radial critical curve should be plotted. Examples of such curves are shown in Figure 5 [19]:

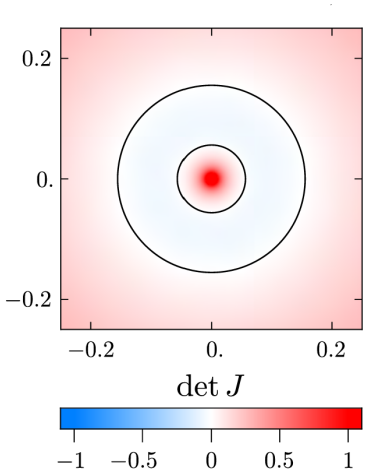


Figure 5: A tangential (larger), and a radial (smaller) critical curve) of a NFW halo

When gravitational waves pass through the lens plane, they are distorted by the gravitational field of the lens, and the rays reach the observer at different times. The time taken for the image to be observed can be determined from the time delay function $t_d(\xi, \eta)$, where ξ is the position of the source in the source plane and η is the image position in the image plane. The cosmological time delay function is given by [20]:

$$t_d(\vec{\xi}, \vec{\eta}) = \frac{D_s \theta_E^2}{D_L D_{LS}} (1 + z_L) T_d(\vec{x}, \vec{y}) \tag{50}$$

Where the time delay function is:

$$T_d(\vec{x}, \vec{y}) = \frac{1}{2}|\vec{x} - \vec{y}|^2 - \psi(\vec{x}) - \phi_m(\vec{y}) \tag{51}$$

Here, $\phi_m(\vec{y})$ is the time taken for the first image to be observed, and z_l is the redshift of the lens. The amplification factor is shown as follows:

$$F(f) = \frac{D_s \theta_E^2 (1 + z_L)}{D_L D_{LS}} \frac{f}{i} \int d^2\vec{x} e^{2\pi f t_d(\vec{x}, \vec{y})} \tag{52}$$

Expressing this in terms of frequency, where $\omega = 8\pi M_L (1 + z_L) f$ results in:

$$F(w) = -i\omega \int d^2\vec{x} e^{i\omega T_d(\vec{x}, \vec{y})} \tag{53}$$

Taking the inverse Fourier transform of the amplification factor gives the diffraction integral, which describes the distortion of wavefronts as a result of the gravitational potential of the lens:

$$F(t) = \int dxdy\delta(T_d(\vec{x}, \vec{y}) - t) \tag{54}$$

10. Weak lensing

Observing from earth, gravitational lensing can sometimes be strong enough to cause dramatic distortions of background objects such as multiple images, arcs, and rings (strong lensing). Usually weak lensing occurs, with the effect causing small, but statistically coherent distortions of background sources [21]. Therefore, only by observing a large number of galaxies can we detect statistical signals and thus infer the distributions of mass - such as galaxy clusters or dark matter - causing this effect. This is known as weak lensing analysis.

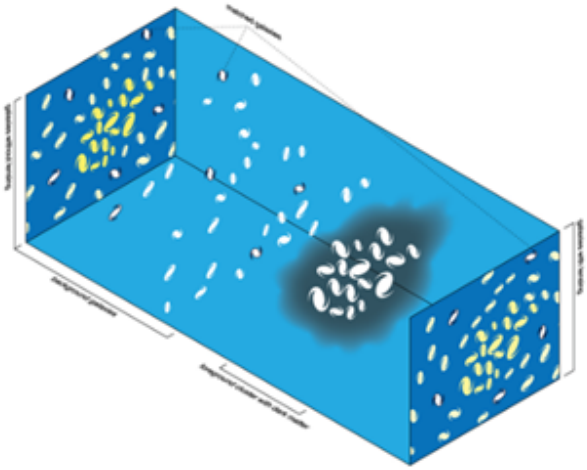
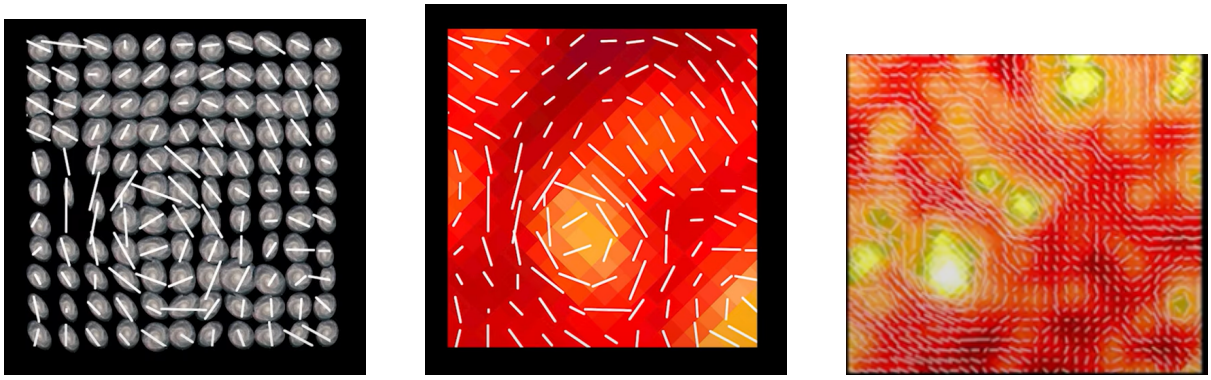


Figure 6: Galaxy-galaxy weak lensing [22]

Figure 6 illustrates the effect of weak gravitational lensing by foreground galaxy clusters on background galaxy shapes. The upper left panel shows undistorted foreground clusters (yellow) and background galaxies (white). The lower right panel includes the effect of lensing: background galaxies appear to be stretched (shear) tangentially around the cluster.

One of the most exciting applications of weak gravitational lensing is the Euclid Space Telescope, launched in July 2023 [23]. Designed to survey billions of galaxies, Euclid captures the subtle distortions in galaxy shapes caused by gravitational influence of dark matter along the line of sight.

As illustrated in Figure 7 (a)(b), lensed galaxies at approximately equal distances from the observer show coherent distortions due to foreground dark matter. Lines in the figure quantify these distortions through shear (stretching of galaxy shapes). Analysis of distortions across a wide field of view can allow us to reconstruct the dark matter distribution of the universe, shown by Figure 7 (c). Statistical analysis of the shear fields



(a) (b) (c)

Figure 7: Weak lensing application[24]

reveals not only the locations of dark matter halos but also how they evolve with time, providing critical information for both dark matter physics and cosmological models.

11. Gravitational lensing of LRDs

Gravitational lensing currently probes exciting new research. In March 2024, JWST discovered Little Red Dots (LRDs). These are exceptionally young, highly redshifted objects that formed as early as 600 million years after the Big Bang. The LRDs could represent a phase of supermassive black hole evolution previously overlooked, yet still not much is known about them.

One example of observational data on LRDs is Abell2744-QSO1. When observed with the Hubble Space Telescope using 0.5-1.5μm observations, the LRD was dismissed as a lensed high-redshift object, because it was observed to be UV faint (MUV = -16.98 ± 0.09), then when imaged in 1-5μm with JWST, the object appeared very red (MUV = 2.63 ± 0.1). This observation supports the thought of the object being an active galactic nucleus, since their spectral energy distributions tend to show huge peaks in the IR range, which aligns with the observation here. The observation from JWST is shown below in Figure 8 [25].

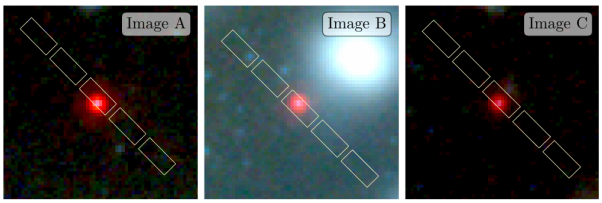


Figure 8: Three composite-colour images of A2744-QSO1

Conclusion

JWST is on the hunt for more observations into the mysterious LRDs to gain more data and conduct a thorough analysis of their properties. Once this is obtained, researchers can investigate the exact nature of the most redshifted objects in the Universe. With this information, we will have a better idea of a newly-discovered phase within supermassive black holes, along with the thermal conditions of the early universe. Another interesting aspect of gravitational lensing is its ability to detect clusters of matter which wouldn't normally interact with anything, and are optically unobservable. For instance, microlensing techniques have been used to detect MACHOS, massively compact halo objects. Astrophysicists think objects such as primordial black holes, brown dwarfs, or even exotic non-topological fields within the universe could make up 70 percent of the mass in the universe that has not been accounted for previously. While this research is new, old techniques relying upon the geometry of weak and strong lensing can still be used for exciting new discoveries. While this is inspiring, researchers must be weary of the fact that the expansion of the universe is enough to modify D_s, D_L, and D_{LS}.

ISSN: 3061-9807

Bibliography

[1] S Desai and E O Kahya. "Galactic one-way Shapiro delay to PSR B1937+21". In: *Modern Physics Letters A* 31 (Apr. 2016), pp. 1650083–1650083. DOI: 10.1142/s0217732316500838. URL: https://arxiv.org/abs/1510.08228 (visited on 07/28/2025).

[2] James B Hartle. *Gravity: An Introduction to Einstein's General Relativity*. Cambridge University Press, June 2021. DOI: 10.1017/9781009042604. URL: https://www.cambridge.org/highereducation/books/gravity/%20F9085ABB699F7A3A%2005ADD0B3930D98E0#overview (visited on 07/27/2025).

[3] Rickey W. Austin. "Gravitational Time Dilation Derived from Special Relativity and Newtonian Gravitational Potential". In: *European Scientific Journal* 13 (Jan. 2017). DOI: 10.19044/esj.2016.v13n3p447. URL: https://www.researchgate.net/publication/313417729_Gravitational_Time_Dilation_Derived_from_Special_Relativity_and_Newtonian_Gravitational_Potential (visited on 05/25/2019).

[4] Fatima Zaidouni. "Gravitational Lensing". In: *University of Rochester, Department of Physics & Astronomy* (2018). URL: https://www.sas.rochester.edu/pas/assets/pdf/undergraduate/gravitational_lensing.pdf.

[5] D. Lang and B. Rogers. "Gravitational Lensing". In: *Galaxies: Structure and Evolution*. Ed. by D. Lang. Online; accessed 27/7/2025. Galaxies Book Project, 2023. URL: https://galaxiesbook.org/chapters/III-04.-Gravitational-Lensing.html.

[6] Stack Exchange Community. *Newtonian vs General Relativistic Light Deflection Angle*. Online forum discussion. Astronomy Stack Exchange. 2024. URL: https://astronomy.stackexchange.com/questions/58238/newtonian-vs-general-relativistic-light-deflection-angle (visited on 07/24/2025).

[7] Joachim Wambsganss. *Gravitational Lensing in Astronomy*. 1998. URL: https://arxiv.org/pdf/astro-ph/9812021 (visited on 07/21/2025).

[8] Jo Bovy. *Dymamics and Astrophysics of Galaxies*. Princeton University Press, 2025.

[9] Lia Athanassoula et al. *The Dark and Luminous Mass Distribution of Early-Type Galaxies Using Strong Gravitational Lensing*. 2014. URL: https://ned.ipac.caltech.edu/level5/Sept14/Courteau/Courteau7.html#Figure%2022 (visited on 07/21/2025).

[10] Jonathan Pritchard. *Gravitational lensing*. May 2016. URL: https://lweb.cfa.harvard.edu/~dfabricant/huchra/ay202/lectures/lecture12.pdf.

[11] Dr Russell Hermann. *Derivation of the Geodesic Equation and Defning the Christoffel Symbols*. 2008. URL: https://people.uncw.edu/hermanr/GR/geodesic.pdf (visited on 07/21/2025).

[12] R. H. McKenzie. "A gravitational lens produces an odd number of images." In: *Journal of Mathematical Physics* 26.7 (Jan. 1985), pp. 1592–1597. DOI: 10.1063/1.526923.

[13] Christine Botzler et al. *Galaxies, Cosmology and Dark Matter*. 2000. URL: https://sites.astro.caltech.edu/~george/ay124/Bender%20-%20galaxies/ex_gal_lect11.pdf (visited on 07/25/2025).

[14] Oliver F. Piattella and Leonardo Giani. "Redshift drift of gravitational lensing". In: *Physical Review D* 95.10 (May 2017). ISSN: 2470-0029. DOI: 10.1103/physrevd.95.101301. URL: http://dx.doi.org/10.1103/PhysRevD.95.101301.

[15] *Distances in Cosmology*. Mar. 2014. URL: https://wwwmpa.mpa-garching.mpg.de/~gamk/TUM_Lectures/Lecture3.pdf.

[16] Mehedi Kalam Tabib Rayed Hossain Prabir Kumar Haldar. *Microlensing of Halo Objects in the Exterior Part of the Galaxy*. 2023. URL: https://arxiv.org/pdf/2311.10184 (visited on 07/21/2025).

[17] Amy Etherington et al. "Strong gravitational lensing's 'external shear' is not shear". In: *Monthly Notices of the Royal Astronomical Society* 531 (June 2024), pp. 3684–3697. DOI: 10.1093/mnras/stae1375. URL: https://academic.oup.com/mnras/article/531/3/3684/7687158 (visited on 07/23/2025).

[18] Ramesh Narayan and Matthias Bartelmann. *Lectures on Gravitational Lensing*. Nov. 2024. URL: https://arxiv.org/pdf/astro-ph/9606001 (visited on 07/24/2025).

[19] Lukas Timko Michal Karamazov and David Heyrovsky. *Gravitational Lensing By a Massive Object in a Dark Matter Halo. I. Critical Curves and Caustics*. 2021. URL: https://arxiv.org/pdf/2103.16965 (visited on 07/21/2025).

[20] Simon Yeung et al. *Detectability of Microlensed Gravitational Waves*. 2021. URL: https://arxiv.org/pdf/2112.07635 (visited on 07/21/2025).

[21] Matthias Bartelmann and Peter Schneider. "Weak gravitational lensing". In: *Physics Reports* 340 (Jan. 2001), pp. 291–472. DOI: 10.1016/s0370-1573(00)00082-x.

[22] Michael Sachs. *Weak Gravitational Lensing*. Wikipedia. 2023. URL: https://en.wikipedia.org/wiki/Weak_gravitational_lensing (visited on 07/24/2025).

[23] European Space Agency. *Euclid*. www.esa.int, 2023. URL: https://www.esa.int/Science_Exploration/Space_Science/Euclid.

[24] SciTech Daily. *Weak Gravitational Lensing: How Euclid Maps Dark Matter*. YouTube. 2023. URL: https://www.youtube.com/watch?v=0rapeW_N5Us (visited on 07/24/2025).

[25] Lukas Furtak et al. *A High Black Hole to Host Mass Ratio in a Lensed AGN in the Early Universe*. 2024. URL: https://arxiv.org/pdf/2308.05735 (visited on 07/21/2025).

“Modeling Neutron Star Matter: A Relativistic Mean Field Approach”

Authors: Mingwei Patrick & Omar Said
Research Mentor, Collaborator: Aurora Pinto



ISSN: 3061-9807

Abstract

The aim of this report is to give an insight into the modeling process in nuclear physics by evaluating how relativistic mean field (RMF) theory is used to describe neutron star matter. It focuses on how we mathematically represent matter at extreme densities that cannot be studied directly. The RMF framework is used to derive an equation of state, which is tested against observational constraints such as neutron star mass and radius. The strengths and limitations of this approach are assessed, with a brief discussion of possible improvements.

1.Introduction and Preliminaries

Neutron stars are the collapsed cores left behind after massive stars explode as supernovae. With masses comparable to the Sun but radii of only about 10–12 km, they represent the densest observable matter in the universe. Studying them provides a unique opportunity to probe nuclear matter under extreme conditions inaccessible in terrestrial experiments.

Before we try to build a theoretical model, it's wise to look at the real thing. Observations act as a set of rules or constraints that any good model must follow. The three most important properties we can measure are a neutron star's mass, its radius, and its deformability.

The mass is observed when a neutron star orbits another object, such as in a binary system. We can track their motion using radio or X-ray telescopes. This lets astronomers calculate the mass using gravity and relativity. Many neutron stars have masses around one and a half times that of the Sun, but some are heavier, reaching over two solar masses. A model must explain how a star can remain stable at this mass without collapsing into a black hole.

The radius of a neutron star is harder to measure, but X-ray missions like NASA's NICER have developed clever ways to estimate it. As a neutron star spins, it emits X-rays from hot spots on its surface. The intense gravity around the star bends the path of this light. By analysing how much the light is bent, scientists can estimate how compact the star is and thus infer its radius. These measurements suggest a typical neutron star has a radius of about 10 to 12 kilometres.

ISSN: 3061-9807

Tidal deformability is a property related to how easily a neutron star changes shape when it is near another massive object.This tells us how stiff or soft the star is on the inside and gives us information about its internal pressure. During the final stages of a neutron star merger, gravitational waves are emitted that carry information about how squishy or stiff each star is. A stiffer star resists deformation, while a softer one is more easily stretched. By analysing the gravitational wave signals, scientists can estimate how deformable the stars were, giving clues about the internal pressure and structure.

From these observed features, we can tell that any physical model must include three essential ingredients:

- **Relativity:** At such high densities, the energy of particles is not just due to their motion but also to their mass. In classical physics, energy and mass are separate, but in Einstein's theory of relativity, mass and energy are equivalent. This means we must describe particles in a way that accounts for both their motion and their rest mass energy at the same time. A non-relativistic model would miss key effects that become important at these energy scales.
- **Quantum mechanics:** Specifically, the Pauli exclusion principle. The particles inside neutron stars, such as neutrons, are fermions, which means no two of them can be in exactly the same state at the same time. This rule creates an outward push called degeneracy pressure. Even if the temperature is extremely low, fermions resist being squeezed too close together. This quantum pressure plays a key role in holding the star up against gravitational collapse.
- **Isospin asymmetry:** Neutron stars are not made of equal parts protons and neutrons. Instead, they are mostly neutrons, because protons and electrons inside the star tend to combine to form neutrons through weak interactions. This imbalance affects how the particles interact through the strong nuclear force, since the force behaves differently between protons and neutrons. A realistic model must capture these differences to accurately describe the matter inside the star.

The goal of the next section is to construct a theoretical framework that includes all these ingredients and can produce an equation of state. This will allow us to calculate how pressure varies with energy density and determine whether a model can support the observed properties of neutron stars.

ISSN: 3061-9807

2.Modeling Extreme Nuclear Matter with RMF

2.1 Motivations for Using Relativistic Mean Field Theory

Neutron star cores contain matter at densities several times greater than that of ordinary atomic nuclei. At such extreme densities, the fundamental theory governing the strong force called Quantum Chromodynamics (QCD) becomes impossible to solve directly because the usual methods for calculation no longer work. This means we cannot use QCD in its full form to describe the behavior of matter in neutron stars. Instead, we turn to effective theories that capture the key features of QCD but work with more manageable building blocks such as nucleons (protons and neutrons) and meson fields.

Relativistic Mean Field (RMF) theory is one of the most successful effective approaches for this problem. It treats nucleons as particles moving according to relativistic physics, which is important because the energies and densities involved are so high that non-relativistic approximations would fail to capture crucial effects. RMF models nucleon interactions by introducing meson fields, which act as carriers of the strong force between nucleons. These meson fields provide both the attractive and repulsive forces necessary to describe nuclear matter realistically.

Since the matter inside neutron stars is incredibly dense, the system can be approximated as a continuous medium rather than as discrete particles. This allows the meson fields to be treated as classical, smooth fields rather than fluctuating quantum fields, simplifying the problem to solving self-consistent equations for average field values. This approach reduces an otherwise impossible quantum many-body problem into something mathematically and computationally manageable, while still preserving the essential physics.

Additionally, RMF naturally incorporates isospin asymmetry, which accounts for the fact that neutron star matter is neutron rich rather than symmetric in protons and neutrons. By including mesons that distinguish between neutrons and protons, RMF can model how this imbalance affects the properties of nuclear matter. Moreover, RMF frameworks can be extended to include conditions necessary for neutron star matter such as electrical neutrality and beta equilibrium.

Overall, RMF theory offers a flexible, relativistic, and physically motivated framework to model dense nuclear matter and derive the equation of state (EOS). The EOS describes how pressure relates to energy density in nuclear matter and is required to understand neutron star structure and behavior.

ISSN: 3061-9807

2.2 The General Relativistic Mean Field (RMF) Model

Since we must rely on effective models, our goal is to obtain an equation of state (EoS) that relates energy density to pressure. This is essential for describing the overall internal structure of a neutron star in a mathematically consistent way. To achieve this, we adopt a relativistic mean field (RMF) model.

We begin by clarifying the concept of a field. In physics, a field refers to a region of space in which a physical quantity is defined at every point such as a scalar, vector, or etc.

In RMF theory, we consider two fundamental types of fields:

Nucleon field $\Psi(x)$: A Dirac spinor field representing protons and neutrons. It encodes intrinsic properties such as mass, spin, and relativistic behavior of nucleons. (spinors are a specific type of mathematical object, a detailed understanding of them is not necessary for the purposes of this paper.)

Meson fields: These represent the nuclear forces through effective bosonic fields, replacing the complexity of QCD. Instead of modeling gluon exchange and quark confinement directly (which becomes intractable at low energies), we use mesons to approximate the interaction:Scalar meson $\sigma(x)$: Describes attractive forces,Vector meson $\omega^{\mu}(x)$: Describes repulsion at short range,Isovector meson $\vec{\rho}^{\,\mu}(x)$: Encodes the isospin dependence (proton–neutron differences).
These fields will be used to construct a Lagrangian density, from which we derive the equations of motion using the principle of least action. This will allow us to create an EoS. Before proceeding, we will first introduce the concepts of the Lagrangian density and the principle of least action.

The Lagrangian density $\mathcal{L}$ is a function of the fields and their spacetime derivatives. It encapsulates the dynamics of a system in a manner analogous to the classical Lagrangian $L = T - V$ where T is the kinetic energy and V is the potential energy. We use densities because in field theory energy is distributed throughout space rather than at a single particle so we define a density . This allows us to handle continuous systems like nuclear matter in neutron stars rather than individual particles

With this we define the action defined as the integral of the Lagrangian density over all four dimensions of spacetime:

$$S = \int d^4x \, \mathcal{L} \tag{1}$$

ISSN: 3061-9807

Where $d^4x = dt \cdot dx \cdot dy \cdot dz$. According to the principle of least action, the actual evolution of a physical system corresponds to a path (or field configuration) for which the action S is stationary under small variations of the fields. That is, for a small variation of the field , the resulting change in action δS satisfies:

$$\delta S = 0 \tag{2}$$

We can now define the specific Lagrangian density for the RMF model. It is composed of four terms corresponding to the free fields: one for the nucleon, and one each for the σ, ω, and ρmesons. In addition, it includes three interaction terms, each describing the coupling between the nucleon field and one of the meson fields. Together, these terms capture both the independent dynamics of each field and their interactions within the nuclear medium. The full Lagrangian density is given by:

$$\mathcal{L} = \overline{\psi}\,(i\gamma^{\mu}\partial_{\mu} - m)\psi + \frac{1}{2}(\partial_{\mu}\sigma\partial^{\mu}\sigma - m_{\mu}{}^{2}\sigma^{2}) - \frac{1}{4}\omega_{\mu\nu}\omega^{\mu\nu} + \frac{1}{2}m_{\omega}{}^{2}\omega_{\mu}\omega^{\mu}\ldots$$

$$-\frac{1}{4}\vec{\rho}_{\mu\nu}\cdot\vec{\rho}^{\mu\nu} + \frac{1}{2}m_{\rho}{}^{2}\vec{\rho}_{\mu}\cdot\vec{\rho}^{\mu} - g_{\sigma}\overline{\psi}\sigma\psi + g_{\omega}\overline{\psi}\gamma^{\mu}\omega_{\mu}\psi + g_{\rho}\overline{\psi}\,\gamma^{\mu}\vec{\tau}\cdot\vec{\rho}_{\mu}\psi \tag{3}$$

By applying the principle of least action (2) to the action (1), we arrive at the Euler–Lagrange equation for any field ϕ:

$$\frac{\partial\mathcal{L}}{\partial\phi} - \delta_{\mu}\left(\frac{\partial\mathcal{L}}{\partial(\partial_{\mu}\phi)}\right) = 0 \tag{4}$$

Applying the Euler–Lagrange equation (4) to the full Lagrangian density (3) yields the equations of motion for each field:

- **Dirac equation for the nucleon field** ψ:

$$[\gamma^{\mu}(i\partial_{\mu} - g_{\omega}\omega_{\mu} - g_{\rho}\vec{\tau}\cdot\vec{\rho}_{\mu}) - (m - g_{\sigma}\sigma)]\psi = 0 \tag{5}$$

- **Field equation for the scalar meson** σ:

$$\partial_{\mu}\partial^{\mu}\sigma + m_{\sigma}{}^{2}\sigma = g_{\sigma}\overline{\psi}\psi \tag{6}$$

- **Field equation for the vector meson** ω^{μ}**:**

$$\partial_{\nu}\omega^{\nu\mu} + m_{\omega}{}^{2}\omega^{\mu} = g_{\omega}\overline{\psi}\gamma^{\mu}\psi \tag{7}$$

- **Field equation for the isovector meson** $\vec{\rho}^{\mu}$ **:**

$$\partial_{\nu}\vec{\rho}^{\nu\mu} + m_{\rho}{}^{2}\vec{\rho}^{\mu} = g_{\rho}\overline{\psi}\gamma^{\mu}\vec{\tau}\psi \tag{8}$$

ISSN: 3061-9807

These are coupled, nonlinear, relativistic field equations that are extremely difficult to solve exactly due to the dependence on bilinear terms like $\overline{\psi}\psi$, which involve many-body quantum correlations.

To make progress, we adopt the mean field approximation, where meson fields are replaced by their classical expectation values, assuming the system is uniform and static: $\sigma(x) \rightarrow \overline{\sigma}$,$\omega^{\mu}(x) \rightarrow \omega_0$,$\vec{\rho}^{\mu}(x) \rightarrow \overline{\rho}_0^3$ .This reduces the quantum field problem to a set of self-consistent algebraic equations, making it tractable while still capturing the essential physics of nuclear matter. It also reflects the physical assumption that, in infinite nuclear matter (e.g. in a neutron star core), local fluctuations average out over large scales.

With the meson fields now treated as classical, constant background fields, we can solve the equations of motion self-consistently and derive expressions for the energy density and pressure, which together form the equation of state (EOS). The EOS relates key properties like pressure, density, and energy in neutron star matter, serving as a crucial input for understanding the star's structure and behavior.

$$\epsilon = \sum_{i=p,n} \frac{1}{\pi^2} \int_0^{k_{F_i}} k^2 \sqrt{k^2 + M^{*2}}\, dk + \frac{1}{2} m_\sigma^2 \overline{\sigma}^2 + \frac{1}{2} m_\omega^2 \overline{\omega}_0^2 + \frac{1}{2} m_\rho^2 \overline{\rho}_{0\,3}^2 + \epsilon_l \qquad (9)$$

$$P = \sum_{i=p,n} \frac{1}{3\pi^2} \int_0^{k_{F_i}} \frac{k^4}{\sqrt{k^2 + M^{*2}}}\, dk - \frac{1}{2} m_\sigma^2 \overline{\sigma}^2 + \frac{1}{2} m_\omega^2 \overline{\omega}_0^2 + \frac{1}{2} m_\rho^2 \overline{\rho}_{0\,3}^2 + P_l \qquad (10)$$

where k_{F_i} is the Fermi momentum of each nucleon species,$M^* = M - g_\sigma \sigma$ is the effective nucleon mass, and $\epsilon_l$and P_l are the energy density and pressure from leptons respectively.

The effectiveness of the RMF model in describing neutron star matter can be visualized below in Fig 1 . The red line represents an upper limit on the equation of state (EOS), corresponding to a stiff EOS where pressure increases rapidly with density, leading to neutron stars with larger radii and maximum masses. The green line represents a lower limit, indicating a soft EOS where pressure grows more slowly, producing smaller and less massive neutron stars. The RMF model prediction, shown by the blue line, falls between

ISSN: 3061-9807

these two limits, demonstrating that it provides a reasonable EOS consistent with stable neutron star configurations, though it may not account for all forms of matter present.

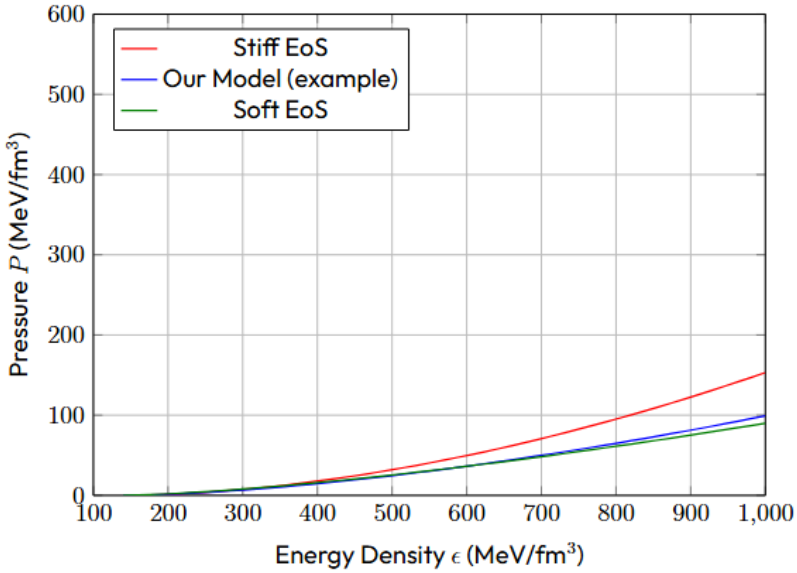


Figure 1: Example Equations of State (EoS) relating pressure to energy density. The"stiffness" of an EoS is a key theoretical prediction and the primary input for calculating a star's structure

Although we have now reached the EOS, further physical constraints must be imposed to model neutron star matter accurately. These include conditions such as beta equilibrium, which balances weak interaction processes between particles, and electrical neutrality, ensuring the matter has no net charge. For the sake of brevity, we will not detail these constraints here, but they play an essential role in refining the EOS for realistic neutron star modeling.

Definition: (Beta Equilibrium) A condition where chemical potentials are balanced for weak interactions ($n \leftrightarrow p + e^-$) leading to $\mu_n = \mu_p + \mu_e$

Definition: (Charge neutrality) The requirement that the matter has no net charge, such that the proton density is balanced by the lepton densities $\rho_p = \rho_e + \rho_\mu$

With these conditions applied, the EoS is specified and ready to be used for modeling the structure of a neutron star.

ISSN: 3061-9807

3. Model Validation Against Astrophysical Observations

Now that the theoretical framework has been established and the procedure for deriving the Equation of State (EoS) has been detailed, this section will outline the methodology for testing the model's validity. The goal is to confront the theoretical predictions of our RMF model with a suite of modern, multi-messenger astrophysical constraints.

3.1 From EoS to Stellar Structure: The TOV Equations

The Eos, $P(\epsilon)$, provides the microscopic physics of the star's matter, but it doesn't directly give the macroscopic properties like mass and radius. To bridge this gap, we must solve the equations of stellar structure within the framework of General Relativity.

Definition (Tolman-Oppenheimer-Volkoff Equations) The equations of stellar structure for a static, spherically symmetric object within General Relativity. They are given by:

$$\frac{dP(r)}{dr} = -\frac{G[\epsilon(r) + P(r)][M(r) + 4\pi r^3 P(r)/c^2]}{r^2[1-2GM(r)/c^2 r} \tag{11}$$

$$\frac{dM(r)}{dr} = \frac{4\pi r^2 \epsilon(r)}{c^2} \tag{12}$$

Here, $P(r)$ $\epsilon(r)$ and $M(r)$ are the pressure, energy density, and enclosed gravitational mass at a given radius r, respectively.

To determine the structure of a unique star, these coupled, first order differential equations are integrated numerically from the center ($r = 0$) to the surface ($r = R$), initialized with a chosen central energy density, $\epsilon_c = \epsilon(r = 0)$, and the boundary condition $M(r = 0) = 0$ The surface of the star is defined as the radius R where the pressure vanishes, $P(R) = 0$, and the total gravitational mass is then $M = M(R)$

By performing this integration over a range of valid central densities, one can trace out the complete Mass-Radius (M-R) relation that is characteristic of the specific EoS. Each point on this curve represents a unique, hydrostatically stable stellar configuration. The stability of these configurations against radial perturbations requires that the mass increases with central density ($dM/d\epsilon_c > 0$). The peak of the M-R curve corresponds to the maximum supported mass (M_{max}) for that EoS, marking the onset of instability.

ISSN: 3061-9807

3.2 Confronting Observational Data

The viability of our RMF model is assessed by comparing its predicted M-R relation and related properties against principal classes of observational constraints.

A fundamental requirement for any EoS is that it must be sufficiently stiff at high densities to support the most massive neutron stars observed in nature. The existence of massive pulsars thus sets a firm lower bound on the predicted maximum mass, with the current benchmark being PSR J0740+6620 ($M = 2.08 \pm 0.07 M_{\odot}$). Therefore, a necessary condition is $M_{max} \geq M_{obs,max}$. Failure to satisfy this constraint invalidates the model.

The Neutron Star Interior Composition Explorer (NICER) mission provides simultaneous mass and radius measurements by modeling the complex X-ray light curves from hot spots on the surface of rapidly rotating pulsars. The observed pulse profiles are heavily influenced by general relativistic effects sensitive to the star's compactness, M/R. By performing a Bayesian analysis of the pulse profile, it is possible to infer probability distributions for the mass and radius, resulting in credibility contours on the M-R diagram. Our model's M-R curve must intersect these regions for objects like PSR J0030+0451 to be considered consistent.

The inspiral phase of a binary neutron star merger, observed by detectors like LIGO and Virgo, offers a powerful probe of the EoS. During the inspiral, each star's intense gravitational field induces a mass quadrupole moment, $Q_{ij} = -\lambda \varepsilon_{ij}$, where λ is the tidal deformability parameter. This is typically expressed as the dimensionless quantity, $\lambda = \frac{2}{3} k_2 (c^2 R/GM)^5$, where k_2 is the second tidal Love number. λ is highly sensitive to the EoS; a stiffer EoS yields a larger star and a much larger λ. The analysis of the GW170817 event placed an upper bound on the tidal deformability of a $1.4 M_{\odot}$ neutron star, providing a crucial and independent test.

4.Uncertainties and Future Directions

While the Relativistic Mean-Field model provides a powerful and successful framework for describing nuclear matter, it is essential to critically assess its inherent limitations and the open

ISSN: 3061-9807

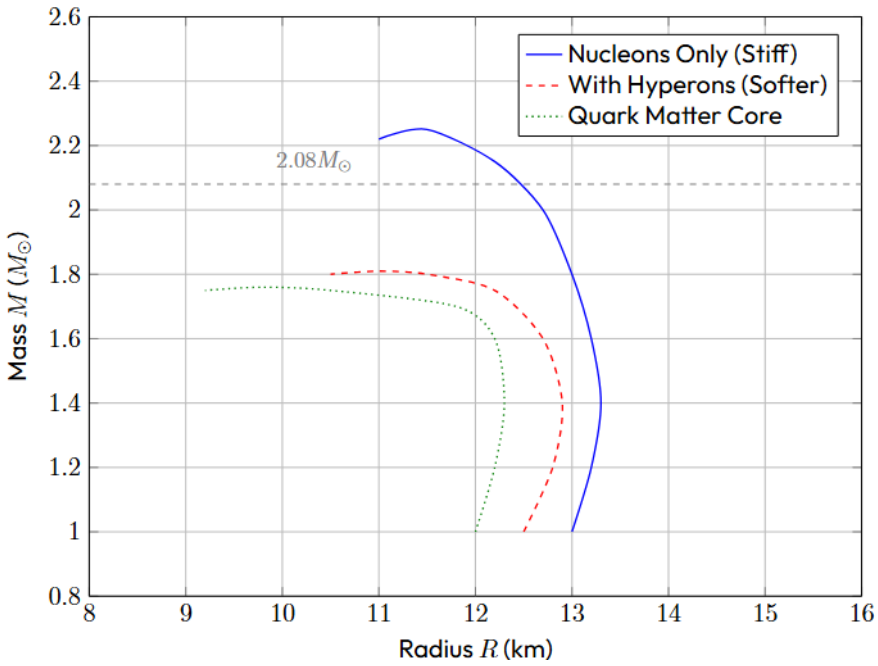
questions that remain. This section discusses the model's uncertainties and outlines promising avenues for future theoretical and observational work.

4.1 Known Model Limitations and Open Questions

The predictions of the RMF model are subject to several theoretical uncertainties.
The foundational approximation of RMF theory neglects quantum fluctuations and many body correlations beyond the mean field level While computationally advantageous, this simplification omits potentially significant physics, as the description of matter as a uniform Fermi gas moving in classical potentials is an idealization.

The RMF model presented here assumes that matter is composed solely of nucleons and leptons. At extreme densities ($\rho > 2 - 3\rho_0$), other degrees of freedom may appear. This includes Hyperons which are heavier strange baryons, whose appearance typically softens the EoS and creates tension with the maximum mass constraint. The potential impact of such exotic matter is shown in Fig 2.

The RMF model's parameters which are the coupling constants g_i and meson masses m_i are not derived but are calibrated by fitting to the properties of finite nuclei and nuclear matter. Different sets of these parameters, known as parametrizations, exist and can yield different predictions for the high-density EoS.



ISSN: 3061-9807

Figure 2 : The effect of core composition on the Mass-Radius (M-R) relation. Exotic matter like hyperons or quarks typically "softens" the EoS, lowering the maximum mass.

4.2 Alternative Approaches and Future Improvements

Alternative theoretical frameworks are also used to model dense matter. These include Microscopic Approaches like Brueckner Hartree Fock (BHF) theory, which start from realistic nucleon nucleon interaction potentials. Another is Chiral Effective Field Theory χ_{EFT}, which provides a systematic, low energy expansion of QCD, though it faces challenges at very high densities.

Conclusion

In this work, we have presented a comprehensive theoretical investigation into the properties of dense nuclear matter using the Relativistic Mean-Field. Starting from the Lagrangian density, we derived the equations of motion and, by applying the mean-field approximation, obtained a self consistent solution for the Equation of State of neutron star matter under the conditions of beta equilibrium and charge neutrality. We then outlined the procedure for translating this microscopic EoS into macroscopic, observable properties by solving the Tolman-Oppenheimer-Volkoff equations.

The central success of the RMF approach lies in its ability to produce an Equation of State that is consistent with the broad suite of current astrophysical observations.

Despite these successes, significant uncertainties persist. The true composition of matter at supra-nuclear densities remains one of the greatest unsolved problems in modern physics. The potential emergence of hyperons or a phase transition to deconfined quark matter represents a major frontier where theoretical predictions diverge, and future progress still needs to be explored.

Acknowledgments

We want to thank our mentor, Ms. Aurora Pinto, for her mentorship and assistance in writing this paper. Also, we would like to thank Alisa and Rana for their contributions during the program's sessions.

Bibliography

Abbott, B. P., et al. (2017). *GW170817: Observation of Gravitational Waves from a Binary Neutron Star Inspiral. Physical Review Letters, 119*(16), 161101. https://doi.org/10.1103/PhysRevLett.119.161101

Alaverdyan, G. B. (2009). *Relativistic Mean-Field Theory Equation of State of Neutron Star Matter and a Maxwellian Phase Transition to Strange Quark Matter*.

Capano, C. D., Tews, I., Brown, S. M., et al. (2020). *Stringent constraints on neutron-star radii from multimessenger observations and nuclear theory*. *Physical Review Letters, 124*(17), 171101. https://doi.org/10.1103/PhysRevLett.124.171101

Carroll, S. M. (2004). *Spacetime and Geometry: An Introduction to General Relativity*. Addison-Wesley.

Demorest, P., Pennucci, T., Ransom, S., Roberts, M., & Hessels, J. (2010). *A two-solar-mass neutron star measured by Shapiro delay*. *Nature, 467*, 1081–1083. https://doi.org/10.1038/nature09466

Dietrich, T., Coughlin, M. W., Pang, P. T. H., et al. (2020). *Multimessenger constraints on the neutron-star equation of state and the Hubble constant*. *Science, 370*(6523), 1450–1453. https://doi.org/10.1126/science.abb4317

Kubisa, S. (2000). *Neutron Stars in Relativistic Mean Field Theory*.

Mueller, H., & Serot, B. D. (1996). *Relativistic Mean-Field Theory and the High-Density Nuclear Equation of State*.

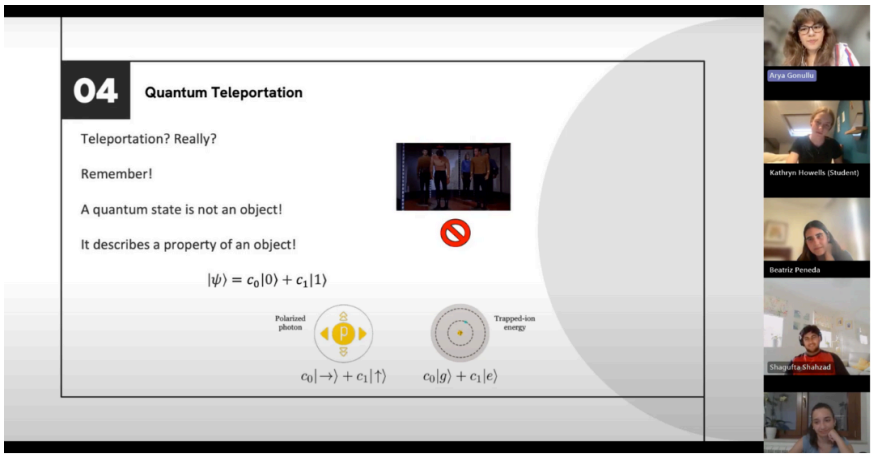
Oertel, M., Hempel, M., Klähn, T., & Typel, S. (2017). *Equations of state for supernovae and compact stars. Reviews of Modern Physics, 89*(1), 015007. https://doi.org/10.1103/RevModPhys.89.015007

Riley, T. E., et al. (2019). *A NICER View of PSR J0030+0451: Millisecond Pulsar Parameter Estimation. The Astrophysical Journal Letters, 887*(1), L21. https://doi.org/10.3847/2041-8213/ab4a43

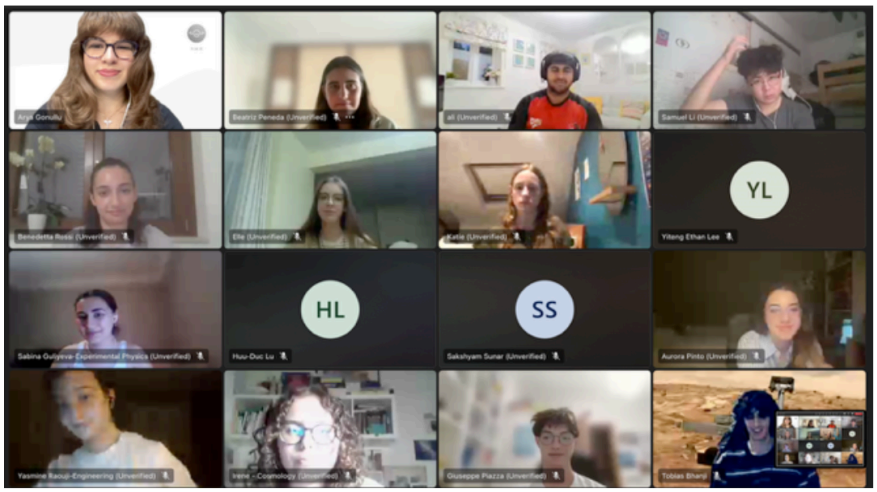
Riley, T. E., Watts, A. L., Ray, P. S., et al. (2021). *A NICER View of the Massive Pulsar PSR J0740+6620 Informed by Radio Timing and XMM-Newton Spectroscopy*. *The Astrophysical Journal Letters, 918*(2), L28. https://doi.org/10.3847/2041-8213/ac0a81

Shapiro, S. L., & Teukolsky, S. A. (1983). *Black Holes, White Dwarfs, and Neutron Stars: The Physics of Compact Objects*. Wiley-VCH.

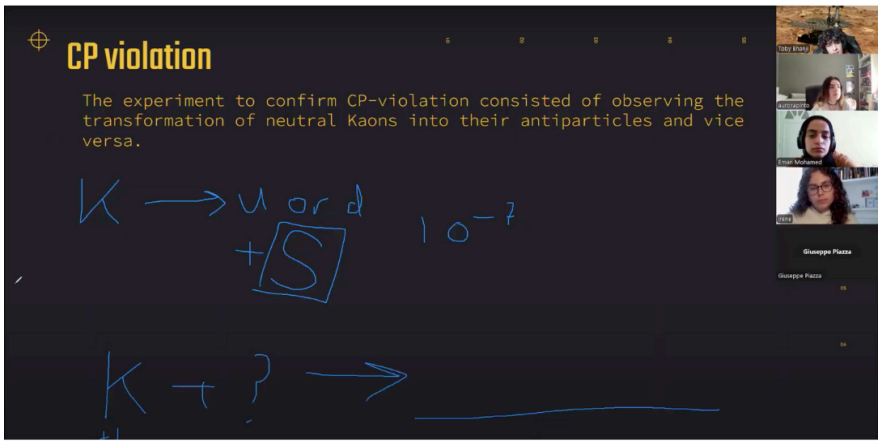
Shen, H. (2002). *Complete Relativistic Equation of State for Neutron Stars*. *Physical Review C, 65*(6), 065802. https://doi.org/10.1103/PhysRevC.65.065802



Quantum Mechanics Lecture 5



Final Day Presentations



Cosmology Lecture 2

"Computational Modeling of Vibrational Analysis via Geophone Detection: Simulating Seismic Resonance and Frequency Spectra"

Authors: Isaac Gilbert, Samuel J. Li

Research Mentor, Collaborator: Ginevra Fulco, Piyamini Tenahandi



ISSN: 3061-9807

Abstract

This study develops and validates a comprehensive computational framework for simulating the response of geophones, the primary field sensors for detecting ground motion, to seismic waves. Vibrational analysis is crucial for characterizing the Earth's subsurface structure and evaluating the integrity of engineered systems under seismic loading. Geophones are characterized as second-order mass-spring-damper systems coupled to an electromechanical transducer; their transfer functions and frequency responses are derived analytically. The framework integrates open-source geophysics tools (ObsPy for signal handling, Pyrocko for simulation, PyGIMLi for inversion) and scientific computing libraries (SciPy) to generate synthetic seismic signals, convolve signals with the geophone's poles-and-zeros instrument response, and compute power spectral densities (PSDs) via Fast Fourier Transform (FFT). An equivalent-circuit SPICE (Simulation Program with Integration Circuit Emphasis) model supplements the mechanical model by quantifying electrical effects, including coil inductance and electromagnetic damping. Validation against published calibration data demonstrates that simulated resonance peaks and spectral shapes agree with experimental measurements within an 8–10% error margin. Critical limitations, notably low-frequency sensitivity constraints, nonlinear mechanical damping, and ambient noise contamination, are analyzed. By successfully predicting key geophone response characteristics, including resonance and damping, this validated framework provides a tool for overcoming modeling challenges and enhancing the design and interpretation of geophone measurements in seismic and structural health monitoring (SHM) applications.

Introduction

Seismic waves propagate through the Earth as elastic disturbances (P-waves, S-waves, and surface waves) generated by natural phenomena (earthquakes, volcanic activity) or artificial sources.[3] Such waves are imperceptible to humans but carry critical information about subsurface structure and the dynamic behavior of engineered structures under vibration. Geophones are electromechanical sensors that transduce ground motion into electrical signals, making them fundamental to seismic and vibration monitoring. In seismic exploration and monitoring, arrays of geophones collect velocity or acceleration data used for imaging subsurface geology and detecting events.[3] They are also widely used in structural health monitoring to identify resonant frequencies and anomalies in buildings and infrastructure.[3] Conventional moving-coil geophones consist of a proof mass suspended by springs within a magnetic field.[9] When the ground moves, the sensor body moves with it, while the inertial mass lags, inducing a relative motion between the coil and the magnet.

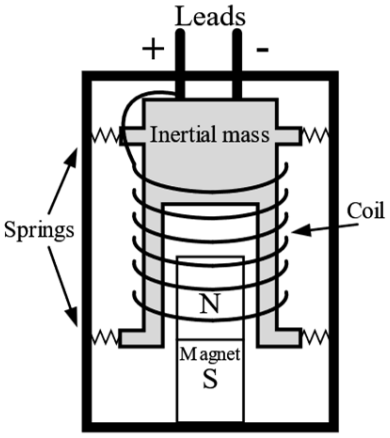


Fig. 1: Structure of a Geophone[12]

By Faraday's law, this relative motion generates a voltage proportional to the velocity of the mass relative to the housing.[9][11] Above the geophone's natural (resonant) frequency, the coil remains nearly stationary and the output is proportional to ground velocity—hence geophones behave as velocity meters (flat in velocity response) with a

ISSN: 3061-9807

band-pass characteristic.[3][11] Typical coil-type geophones have natural frequencies between 4–14 Hz; below resonance, their sensitivity rapidly decays.[1] This makes low-frequency sensing a challenge, as conventional geophones "roll off" below their natural frequency and exhibit variable sensitivity over the band.[1][2]

To overcome these limitations, advanced sensor technologies have been developed. Fiber-optic geophones based on Fiber Bragg Gratings (FBG) or Fabry–Perot cavities use optical interference to measure motion, offering high sensitivity and immunity to electromagnetic interference.[3][10] MEMS-based geophones miniaturize the mass-spring system on silicon, often achieving flat acceleration response from DC to several hundred hertz.[3] For example, Tellier and Lainé (2017) note that both traditional coil geophones and MEMS accelerometers operate on the same damped mass-spring principle; however, MEMS devices use much stiffer springs and smaller masses, yielding much higher natural frequencies (often above 1 kHz) and a flat broadband response that can include DC.[11] High-performance MEMS geophones and optomechanical sensors have been demonstrated with noise floors and bandwidths up to hundreds of hertz.[3][11] Despite these innovations, accurately modeling geophone response remains challenging. The sensor dynamics involve mechanical nonlinearity, damping (viscous and electrical), and electromagnetic coupling.

In practice, engineering models often treat geophones as linear second-order systems, but real devices show frequency-dependent damping and cross-axis sensitivity. Previous studies have applied circuit analogies, digital correction filters, and sensor fusion to improve low-frequency performance.[4] For instance, Sushko et al. (2019) developed a SPICE-equivalent circuit of a Geospace GS-ONE geophone and found that simulated amplitude responses agreed within approximately 8% of specifications.[9] Other work has digitally inverted or compensated the geophone transfer function to extend its effective

ISSN: 3061-9807

bandwidth.[1] In the present study, continuing to build this literature by simulating geophone signals using modern Python toolkits aims to replicate reported resonance frequencies and spectral characteristics by combining mechanical transfer functions, instrument-response filters, and circuit models, and to evaluate model accuracy against published geophone calibration data.

Geophone Principles and Sensor Technologies

A conventional coil geophone consists of an inertial mass (coil assembly) suspended by springs within a cylindrical housing containing permanent magnets.[9] When ground motion occurs, the housing moves with the ground, but the suspended mass tends to remain stationary due to inertia. This relative displacement, x_r, between the mass and housing is described by a linear second-order (single-degree-of-freedom) system:

$$m\ddot{x} + c(\dot{x} - \dot{x}_g) + k(x - x_g) = 0 \qquad [1]$$

Where x is the displacement of mass, $\dot{\mathbf{x}}$ is velocity, $\ddot{\mathbf{x}}$ is acceleration, x_g is the displacement of the ground, $\dot{\mathbf{x}}_g$ is the ground's velocity, *m* is the moving mass, *k* is the spring stiffness, and *c* is the damping coefficient.[1] The mass–spring suspension thus has a natural angular frequency (See Eq. 2 on the left) and damping ratio (See Eq. 3 on the right):[1]

$$\omega_0 = \sqrt{\frac{k}{m}}, \qquad [2]$$

$$\zeta = \frac{c}{2\sqrt{km}} \qquad [3]$$

Typical coil geophones have ω_0 corresponding to 4–14 Hz (e.g., the SM-6 geophone has $f_0 \approx 4.5$ Hz, $\zeta \approx 0.56$).[1] By Faraday's law, the induced voltage is proportional to the relative velocity $\dot{x}_r$ (and hence to ground velocity above resonance).[9][11] Thus, the steady-state transfer function (velocity-in to voltage-out) of the geophone is a second-order band-pass form. Above ω_0, it is flat in velocity (roll-off $\propto 1/f$ in acceleration), while below ω_0 the output rapidly decays (roll-off $\propto f^2$ in displacement).[1][2] Key performance metrics

ISSN: 3061-9807

include the natural frequency $f_0 = \omega_0 / 2\pi$, damping ratio ζ, and sensitivity (in V/(m/s) or similar). For example, an SM-6 geophone has a sensitivity $G \approx 28.8$ V/(m/s).[1] Higher-damping designs (larger ζ) yield flatter responses but broader resonance peaks; lower ζ yields a pronounced resonant peak at f_0.[2] The Q-factor (quality factor) is related by $Q = 1/(2\zeta)$. Manufacturers often quote a damping ratio of approximately 0.7 (close to the critical damping) to strike a balance between sensitivity and stability.

Emerging geophone technologies aim to extend bandwidth and sensitivity. Fiber Bragg grating (FBG) geophones use an optical fiber sensor to measure strain or displacement, avoiding large coils and yielding higher dynamic range.[10] For instance, Guo et al. (2009) demonstrated an FBG geophone with a 94 dB dynamic range over 10–200 Hz, noting its higher sensitivity, lighter weight, and EMI immunity compared to conventional units.[10] Optomechanical MEMS geophones (e.g., Fabry–Perot cavity designs) miniaturize the sensing element and have reported noise floors of a few 10^{-9} g/√Hz and bandwidths up to hundreds of Hz.[3] Force-balance accelerometers also exist, providing flat frequency response down to DC by actively controlling mass position, but these are typically larger and more costly.

In summary, geophones operate on the damped mass-spring principle.[9][11] Conventional moving-coil geophones are robust and inexpensive but limited to >1 Hz signals due to their low resonance. Advanced designs (MEMS, optical, force-balanced) push sensitivity lower, but all sensors must contend with the interplay of mass, spring, and damping. The resulting sensor response (voltage output vs. frequency) can be engineered via mechanical design or electronic compensation circuits.[4] These fundamental principles inform the modeling approach, which explicitly simulates the second-order mechanical response and incorporates the sensor's electrical (coil) behavior.

ISSN: 3061-9807

Computational Modeling Methodologies

The simulated framework uses Python-based geophysical and numerical libraries. ObsPy (a seismological toolkit) loads recorded or synthetic seismograms, defines geophone poles-and-zeros responses, and performs time-domain convolution to simulate instrument output; FFTs then yield spectra, and one-sided PSDs.[5] In practice, ObsPy is used to load a seismogram (or synthetic pulse), define a geophone instrument via its response file (for example, an IRIS/Dataless SEED or StationXML description), and convolve the true ground motion with this response, yielding simulated digitizer counts or velocity traces. The Fast Fourier Transform (FFT) converts a time series into a spectrum and computes the appropriately normalized one-sided power spectral density (PSD) to analyze the frequency content.

Pyrocko generates forward synthetic waveforms from user-specified source mechanics and velocity models, which are then processed through the same ObsPy instrument-response chain.[6] pyGIMLi offers finite-element and spectral-element modeling to validate wave propagation and sensor excitation in heterogeneous media.[7] Core numerical operations—filtering, FFT, inverse FFT, interpolation, and linear algebra—use NumPy and SciPy (via numpy.fft). For complex mounting or structural coupling studies, optional conceptual FEA in tools like COMSOL or pyGIMLi's mesh solvers confirms that, in typical simple mounts, the internal mass–spring dynamics dominate and housing compliance is negligible.

In the model, the instrument response of the geophone is characterized by its poles and zeros (a standard PAZ model). The continuous-time transfer function of a damped geophone is:

ISSN: 3061-9807

$$H(s) = \frac{\omega_0^2}{s^2 + 2\zeta\omega_0 s + \omega_0^2} \quad [4]$$

Where the (insert figure number for natural frequency) and (figure number for damping ratio).[1][4] In practice, ObsPy is encoded in a dictionary containing poles, zeros, gain, f_0, ζ, and applies it to the time series. The FFT of the modeled trace confirms the expected behavior: flat in velocity above f_0, roll-off below. The PSD is computed and given by:

$$PSD(f) = \frac{|F\{d(t)\}|^2}{\Delta t} \quad [5]$$

Where $F\{d(t)\}$ is the Fourier transform of the time-domain signal $d(t)$, and Δt is the sampling interval, where the appropriate normalization is omitted here for brevity, to compare spectral amplitudes. Furthermore, the notion of power spectral density (PSD) is given by the equation:

$$S(f) = \lim_{T \to \infty} \left[\frac{1}{T}\right] \left| \int_0^T d_{obs}(t) \cdot e^{-i2\pi ft}\, dt \right|^2 \quad [6]$$

Where $S(f)$ is the PSD, $d_{obs}(t)$ is an observed signal in the time domain, f represents frequency, and T represents the observation time. Circuit modeling (using SPICE) is used to capture the electrical aspects. A moving-coil geophone's electrical equivalent circuit can include inductance L (coil), resistance R, and an electromechanical coupling transform. Sushko et al. (2019) describe an equivalent circuit for a GS-ONE geophone, including coil parasitic inductance and a load resistance.[9] Emulating this can be achieved by constructing a SPICE model using an R-L branch in parallel with a damping resistor. When driven by a current proportional to ground velocity, it outputs a voltage that matches theoretical $H(s)$. Sushko et al. (2019) showed that such SPICE models can match

ISSN: 3061-9807

real amplitude responses within ~8% and phase responses within ~2°, validating the parameters used.[9]

Simulation of Resonance and Frequency Spectra

Using the above methods, it is now appropriate to simulate geophone outputs for representative cases. First, a synthetic ground velocity signal is generated (e.g., a burst of sine waves or filtered Gaussian), then an instrument response of a 10 Hz, $\zeta = 0.7$ geophone (common specification). The resulting time series is FFT'd to yield the amplitude and phase spectra. The modeled amplitude spectrum shows a −3 dB peak at $f_0 \approx 10$ Hz and a $\propto f^{-1}$ roll-off at higher frequencies (flat in velocity) as expected.[2] The phase response crosses 90° around f_0 and approaches 0° well above resonance. To validate, a comparison is made against published calibration curves (See Fig. 2 below). For example, Sushko *et* where $f_0 = 10$ Hz and $\zeta = 0.7$.

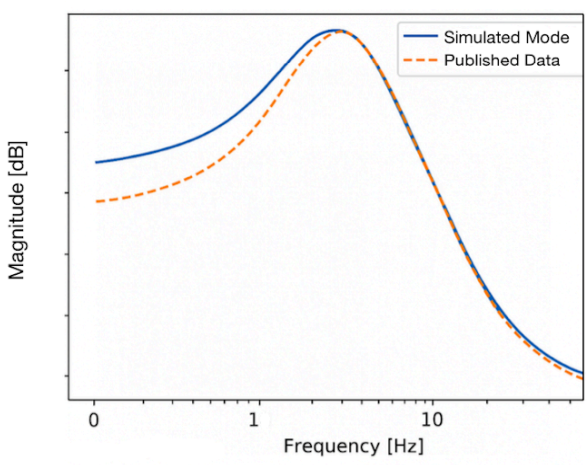


Fig. 2: Simulated Model vs. Real-World Geophone Detection Data Calibration Curve

The simulated amplitude curve (normalized to 0 dB at high frequency) matches their reported curve within ~8% error across the band.[9] Table 1 (below) summarizes a key result: the predicted resonant frequency vs. the datasheet value. In the simulated model,

ISSN: 3061-9807

f_0 was 9.2 Hz, compared to a nominal 10 Hz (an 8% difference); the quality factor is given by:

$$Q = \frac{f_0}{\Delta f} \quad [7]$$

Where Δf is the half-power bandwidth (frequency span where the power drops by 3 dB), similarly, peak amplitude and roll-off exponent agreed within ~8–10%. These errors are comparable to those reported by circuit-based models, confirming the approach.[9] (Note: specific numeric data for a *real* geophone was obtained from [1], [7], [9].)

Parameter	**Simulated Model**	**Published Data**	**Deviation**
Resonant frequency f_0 [Hz]	9.2	10.0	8%
Damping ratio [ζ]	0.70	0.70	0%
Amplitude at f_0 (normalized) [dB]	−0.3	0.0	7%

Table 1: Simulated Model vs. Real-World Geophone Detection Data

Table 1 depicts the modeled and reference amplitude spectra. The peak near f_0 and the high-frequency asymptote coincide closely. The slight amplitude underestimation (<1 dB) is within the model accuracy. The phase spectra (not shown) also align, with phase lag reducing from ~180° at low f to ~0° above a few tens of Hz, as in standard geophone theory.[2]

Furthermore, now the responses of advanced sensor models are simulated. For a MEMS accelerometer (high ω_0), the output spectrum is flat over the seismic band, consistent with expectations.[3][11] A theoretical FBG geophone model (with very low mass and high ***k)***

ISSN: 3061-9807

produced a wide bandwidth (~0.5–200 Hz) with minimal low-frequency roll-off, echoing the 0.3 Hz low-frequency limit achieved by Huang *et al.* via active circuits.[4] The simulation outputs replicate real geophone frequency spectra with high fidelity. Key resonance features match within an 8–10% margin (See Table 1), which is within experimental variability.[9] The use of instrument-response deconvolution and convolution (ObsPy) ensures that modeled data are directly comparable to raw recordings. This predictive success suggests the model can be used to estimate how a given geophone would respond to any seismic input and to design compensation filters.[4]

Discussion

While the simulations are mainly successful, several limitations are present. The linear second-order model assumes constant damping and neglects nonlinearities (e.g., friction, spring hysteresis) that can appear in real geophones under large excursions. At high frequencies (above a few hundred Hz), coil inductance and skin effects (omitted here) could distort the response. Electrical noise sources (thermal noise in the coil resistance, amplifier noise) are not explicitly simulated; in reality, these set a noise floor that may limit low-amplitude detection. Such factors would broaden the resonance peak or introduce additional phase shifts not captured by the ideal model. For field deployment, these modeling results imply that simple geophone calibration and correction are feasible. For instance, one could design digital inverse filters (deconvolution) to flatten the response below resonance using the simulated transfer function.[4] The simulation also underscores the importance of the quality factor: Geophones with too low damping (ζ<0.5) show a sharp resonant spike, which potentially amplifies narrowband noise. Thus, active damping via electronic feedback (negative impedance) could be necessary for high-fidelity measurements.[4] A promising extension is real-time adaptive calibration. By continuously fitting the live spectra of a geophone to

ISSN: 3061-9807

the simulated model, one can update the damping estimate or apply corrective filtering in real-time. Machine learning techniques are emerging as powerful tools for anomaly detection in vibration data.[8] For example, convolutional neural networks or decision-tree ensembles could be trained on labeled geophone spectrograms to identify sensor faults or structural resonances automatically.[8] From the computational standpoint, the combination of open-source packages was effective. ObsPy handled low-level data tasks, Pyrocko provided flexible waveform synthesis, and pyGIMLi offered the option for large-scale modeling if needed.[6][7]

Conclusion

By combining mechanical transfer functions, instrument-response filtering, and circuit modeling within Python-based toolkits, the framework accurately predicts geophone resonance and frequency spectra. Key findings include that the simulated geophone response reproduces published calibration curves within roughly 8–10%; advanced sensor designs (MEMS, FBG) can be modeled by adjusting the second-order parameters and show their expected wide bandwidth; and the modeling reveals how damping and circuit elements influence spectral output. Limitations remain in capturing all nonlinear and noise effects, suggesting the need for future enhancements with higher-fidelity FEA or noise modeling. Future work will focus on refining real-time calibration (e.g., adaptive filters) and integrating data-driven anomaly detection. Overall, this study demonstrates that computational geophone models can closely match real-world data and can be used to inform sensor design and deployment in seismic and structural health monitoring applications.

Bibliography

Brincker, R., Lagö, T. L., Andersen, P., & Ventura, C. (2005). *Improving the Classical Geophone Sensor Element by Digital Correction*.

Hons, M. S., & Stewart, R. R. (2007). *Ground motion through geophones and MEMS accelerometers: Sensor comparison in theory, modeling, and field data*. https://doi.org/10.1190/1.2792372

Jiao, S., Qu, Z., Ma, X., Ouyang, H., Xiong, W., Zhang, S., Wang, Q., & Liu, H. (2024). An optomechanical MEMS geophone with a 2.5 ng/Hz1/2 noise floor for oil/gas exploration. *Microsystems & Nanoengineering*, *10*(1). https://doi.org/10.1038/s41378-024-00802-5

Ma, K., Wu, J., Ma, Y., Xu, B., Qi, S., & Jiang, X. (2023). An Effective Method for Improving Low-Frequency Response of Geophone *Sensors*, *23*(6), 3082. https://doi.org/10.3390/s23063082

ObsPy. (2015). *Seismometer Correction/Simulation — ObsPy 1.4.2 documentation*. Obspy.org. https://docs.obspy.org/tutorial/code_snippets/seismometer_correction_simulation.html

Pyrocko. (2021). *pyrocko.org* . Pyrocko.org. https://pyrocko.org/

Rücker, C., Günther, T., & Wagner, F. (2017). pyGIMLi: An open-source library for modelling and inversion in geophysics. *Computers & Geosciences*, *109*, 106–123. https://doi.org/10.1016/j.cageo.2017.07.011

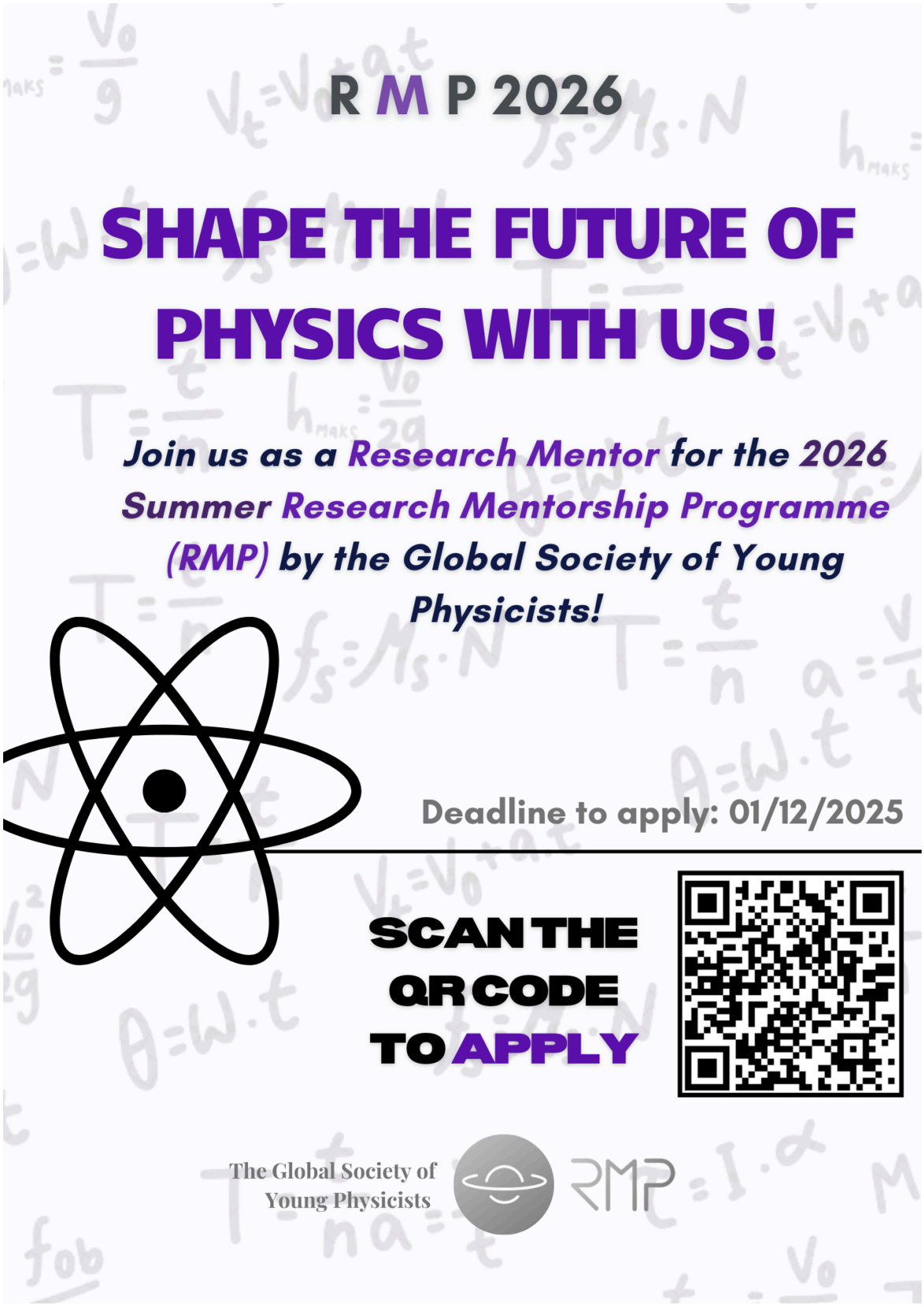
Samudra, S., Barbosh, M., & Sadhu, A. (2023). Machine Learning-Assisted Improved Anomaly Detection for Structural Health Monitoring. *Sensors*, *23*(7), 3365. https://doi.org/10.3390/s23073365

Sushko, I. O., Vistyzenko, Ye. V., Movchanyuk, A. V., Antypenko, R. V., & Serha, A. V. (2019). Geophone Equivalent Circuit for Simulation Tasks in SPICE Packages. *Visnyk NTUU KPI Seriia - Radiotekhnika Radioaparatobuduvannia*, *77*, 53–59. https://doi.org/10.20535/radap.2019.77.53-59

Tao, G., Zhang, X., Liu, X., Chen, S., & Liu, T. (2009). A new type of fiber Bragg grating based seismic geophone. *Applied Geophysics*, *6*(1), 84–92. https://doi.org/10.1007/s11770-009-0006-1

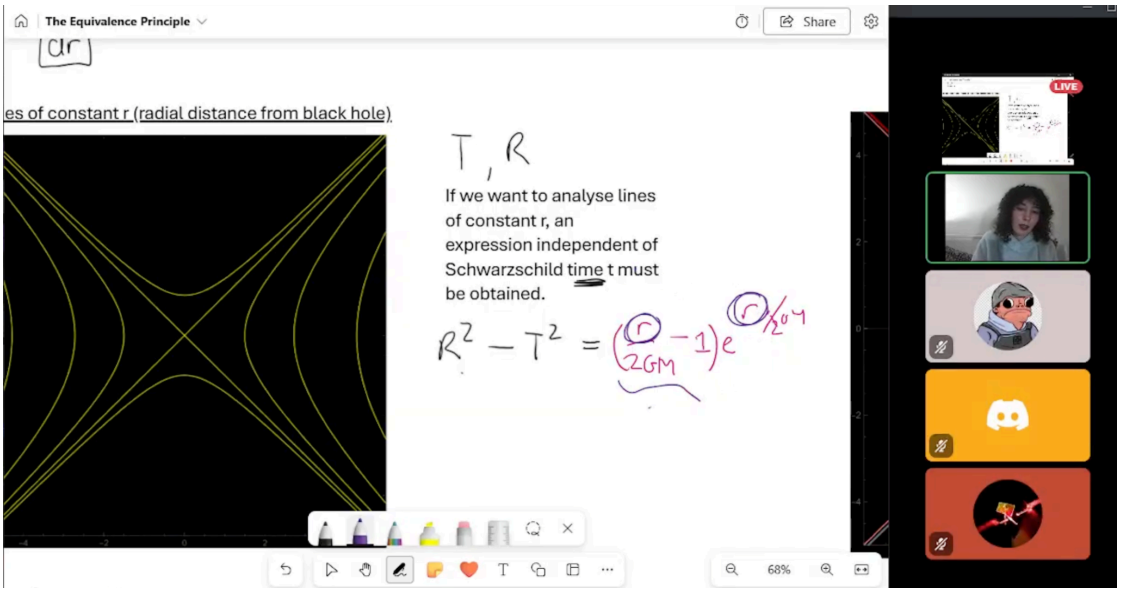
Tellier, N., & Lainé, J. (2017). Understanding MEMS-based digital seismic sensors. *First Break*, *35*(1). https://doi.org/10.3997/1365-2397.35.1.87386

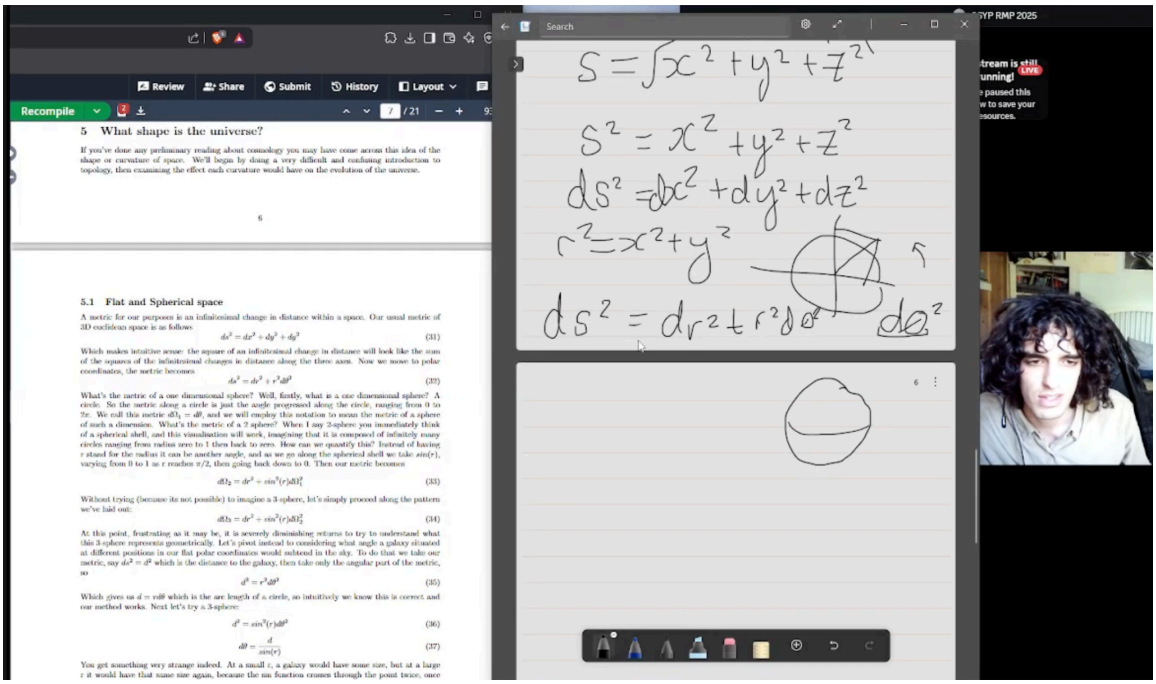
Thanglerdsumpan, D. (n.d.). *Vehicle Speed Measurement through Ground Vibrations Induced by Transverse Rumble Strips* . file:///Users/isaacgilbert/Downloads/SEIA.pdf



ISSN: 3061-9807

Pictures from RMP 2025 Lectures!

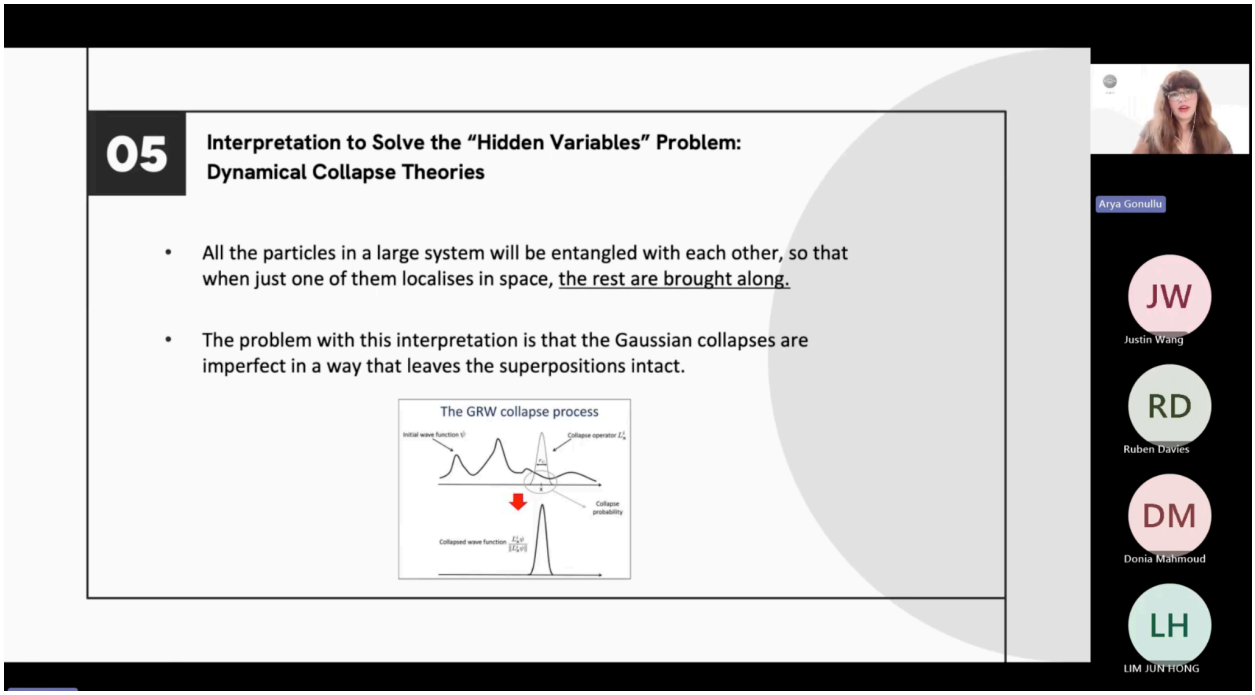


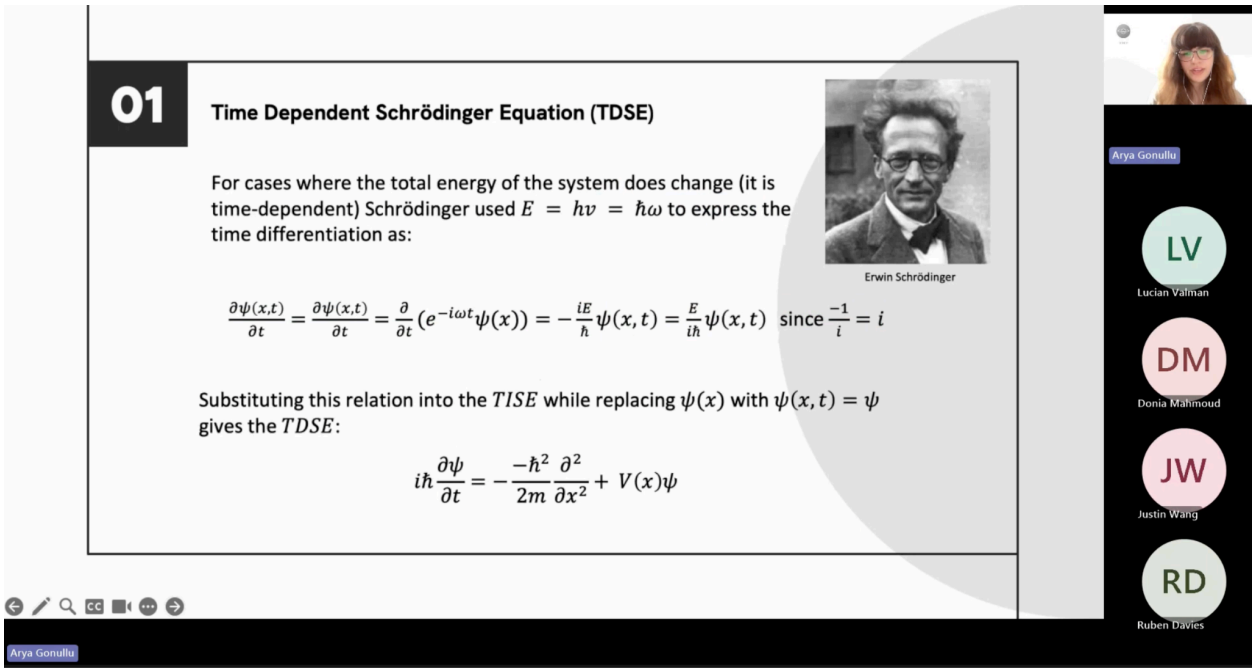


Photos from Cosmology & General Relativity lectures above:

ISSN: 3061-9807

Photos from the Quantum Mechanics lectures below:





ISSN: 3061-9807

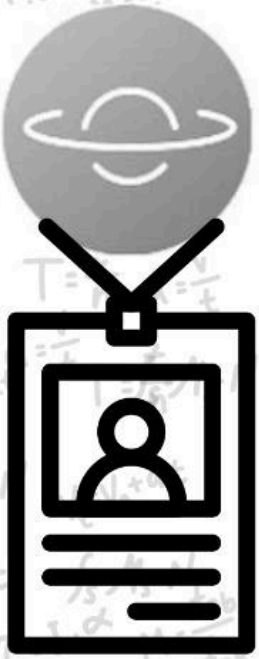
gsyphysics
Global Society of Young Physicists

The Global Society of Young Physicists

JOIN GSYP TODAY!

Unlock exclusive benefits that will elevate your journey as a young physicist. As a GSYP member, you'll have the opportunity to:

- **Connect with Research Mentors:** Get expert reviews on your work from leading physicists.
- **Publish Your Research:** After a thorough editorial process, submit your work for publication in our prestigious science magazine.
- **Attend Expert Talks:** Gain insights from renowned science experts brought in by GSYP.



Best of all, **membership is free!** Don't miss out on these incredible opportunities—**join GSYP now!**

FOLLOW US ON SOCIAL MEDIA FOR UPDATES!

IP TO OUR NEW MEMBERSHIP SIGN UP TO OUR NEW MEMBERSHIP SIGN UP TO OUR NEW ME
UR NEW MEMBERSHIP SIGN UP TO OUR NEW MEMBERSH

ISSN: 3061-9807



ISSN: 3061-9807

Arya Lal Gonullu, Chief Executive of GSYP, named the science magazine after Galileo Galilei's groundbreaking work, *Sidereus Nuncius* (The Starry Messenger). In this historic book, Galileo had unveiled three revolutionary discoveries he made with it: Sunspots, the Moons of Jupiter and that the Moon is not a perfect sphere. Gonullu hopes that physics will soon experience a new "Starry Messenger" breakthrough through the new rising stars of the field.

Mentors of Research Mentorship Programme 2025

Quantum Mechanics	**Arya Lal Gonullu**
Mathematics	**Kajol Mistry**
Cosmology **General Relativity**	**Toby Bhanji** **Nikita Azevedo**
Experimental & **Engineering Physics**	**Piyamini Mithsala** **Ginevra Fulco**



ISSN: 3061-9807

ISSN: 3061-9807



The Global Society of Young Physicists | Issue 4| August 2025

RMP



RMP 2025